

**Research Paper**

**Correspondence to:**  
Vasileios Karakostas  
[vkarak@geo.auth.gr](mailto:vkarak@geo.auth.gr)

**DOI number:**  
<http://dx.doi.org/10.12681/bgsg.27237>

**Keywords:**  
seismic sequence; finite–fault slip model; seismological geodesy; stress transfer and triggering

**Citation:**  
Karakostas, V., Papazachos, C., Papadimitriou, E., Foumelis, M., Kiratzi, A., Pikridas, C., Kostoglou, A., Kkallas, C., Chatzis, N., Bitharis, S., Chatzipetros, A., et al. (2021), The March 2021 Tyrnavos, Central Greece, Doublet ( $M_w6.3$  and  $M_w6.0$ ): Aftershock Relocation, Faulting Details, Coseismic Slip and Deformation. Bulletin Geological Society of Greece, 58, 131–178.

**Publication History:**  
Received: 09/06/2021  
Accepted: 18/08/2021  
Accepted article online: 24/08/2021

The Editor wishes to thank two anonymous reviewers for their work with the scientific reviewing of the manuscript and Ms Emmanouela Konstantakopoulou for editorial assistance.

©2021. The Authors  
This is an open access article under the terms of the Creative Commons Attribution License, which permits use, distribution and reproduction in any medium, provided the original work is properly cited

**THE MARCH 2021 TYRNAVOS, CENTRAL GREECE, DOUBLET ( $M_w6.3$  and  $M_w6.0$ ): AFTERSHOCK RELOCATION, FAULTING DETAILS, COSEISMIC SLIP and DEFORMATION**

Vasileios Karakostas<sup>1</sup>, Constantinos Papazachos<sup>1</sup>, Eleftheria Papadimitriou<sup>1</sup>, Michael Foumelis<sup>2</sup>, Anastasia Kiratzi<sup>1</sup>, Christos Pikridas<sup>3</sup>, Anastasios Kostoglou<sup>1</sup>, Charalambos Kkallas<sup>1</sup>, Nikolaos Chatzis<sup>1</sup>, Stylianos Bitharis<sup>3</sup>, Alexandros Chatzipetros<sup>4</sup>, Aristidis Fotiou<sup>3</sup>, Chrisanthi Ventouzi<sup>1</sup>, Eleni Karagianni<sup>1</sup>, Pavlos Bonatis<sup>1</sup>, Christos Kourouklas<sup>1</sup>, Parthena Paradisopoulou<sup>1</sup>, Emmanouil Scordilis<sup>1</sup>, Domenikos Vamvakaris<sup>1</sup>, Ioannis Grendas<sup>1</sup>, Despoina Kementzetzidou<sup>1</sup>, Areti Panou<sup>1</sup>, George Karakaisis<sup>1</sup>, Ioanna Karagianni<sup>1</sup>, Panagiotis Hatzidimitriou<sup>1</sup>, Odysseas Galanis<sup>1</sup>

<sup>1</sup>Geophysics Department, School of Geology, Aristotle University of Thessaloniki, Greece  
[vkarak@geo.auth.gr](mailto:vkarak@geo.auth.gr), [kpapaza@geo.auth.gr](mailto:kpapaza@geo.auth.gr), [ritsa@geo.auth.gr](mailto:ritsa@geo.auth.gr), [kiratzi@geo.auth.gr](mailto:kiratzi@geo.auth.gr), [akostogl@geo.auth.gr](mailto:akostogl@geo.auth.gr), [chkalla@geo.auth.gr](mailto:chkalla@geo.auth.gr), [chatniko@geo.auth.gr](mailto:chatniko@geo.auth.gr), [xrusven@geo.auth.gr](mailto:xrusven@geo.auth.gr), [elkarag@geo.auth.gr](mailto:elkarag@geo.auth.gr), [mponatis@geo.auth.gr](mailto:mponatis@geo.auth.gr), [ckouroukl@geo.auth.gr](mailto:ckouroukl@geo.auth.gr), [ppara@geo.auth.gr](mailto:ppara@geo.auth.gr), [manolis@geo.auth.gr](mailto:manolis@geo.auth.gr), [dom@geo.auth.gr](mailto:dom@geo.auth.gr), [igrendas@geo.auth.gr](mailto:igrendas@geo.auth.gr), [dkementz@auth.gr](mailto:dkementz@auth.gr), [arpanou@geo.auth.gr](mailto:arpanou@geo.auth.gr), [karakaisis@geo.auth.gr](mailto:karakaisis@geo.auth.gr), [ikara@geo.auth.gr](mailto:ikara@geo.auth.gr), [chdimitr@geo.auth.gr](mailto:chdimitr@geo.auth.gr), [ogalanis@geo.auth.gr](mailto:ogalanis@geo.auth.gr)

<sup>2</sup>Department of Physical and Environmental Geography, School of Geology, Aristotle University of Thessaloniki, Greece,  
[mfoumelis@geo.auth.gr](mailto:mfoumelis@geo.auth.gr)

<sup>3</sup>Department of Geodesy and Surveying, School of Rural and Surveying Engineering, Aristotle University of Thessaloniki, Greece,  
[cpik@topo.auth.gr](mailto:cpik@topo.auth.gr), [stylbith@gmail.com](mailto:stylbith@gmail.com), [afotiou@topo.auth.gr](mailto:afotiou@topo.auth.gr)

<sup>4</sup>Department of Geology, School of Geology, Aristotle University of Thessaloniki, Greece,  
[ac@geo.auth.gr](mailto:ac@geo.auth.gr)

**Abstract**

*On 3 March 2021, the  $M_w6.3$  Tyrnavos earthquake shook much of the Thessalia region, leading to extensive damage in many small towns and villages in the activated area. The first main shock was followed in the next day, on 4<sup>th</sup> of March 2021, by an “equivalent” main shock with  $M_w6.0$  in the adjacent fault segment. These are the largest earthquakes to strike the northeastern part of Thessalia since the  $M6.3$ , 1941*

*Larissa earthquake. The main shocks triggered extensive liquefaction mainly along the banks of the Titarisios tributary where alluvial flood deposits most probably amplified the ground motions. Our seismic monitoring efforts, with the use of recordings of the regional seismological network along with a dense local network that was installed three days after the seismic excitation initiation, led to the improved understanding the geometry and kinematics of the activated faults. The aftershocks form a north–northwest–trending, east–northeast–dipping, ~40 km long distribution, encompassing the two main ruptures along with minor activated structures, consistent with the rupture length estimated from analysis of regional waveform data and InSAR modeling. The first rupture was expanded bilaterally, the second main shock nucleated at its northern tip, where from this second rupture propagated unilaterally to the north–northwest. The focal mechanisms of the two main shocks support an almost pure normal faulting, similar to the aftershocks fault plane solution determined in this study. The strong ground motion of the March 3 main shock was computed with a stochastic simulation of finite fault model. Coseismic displacements that were detected using a dense GPS / GNSS network of five permanent stations located the Thessaly region, have shown an NNE–SSW extension as expected from the nature and location of the causative fault. Coulomb stress changes due to the coseismic slip of the first main shock, revealed that the hypocentral region of the second main shock was brought closer to failure by more than 10 bars.*

**Key words:** seismic sequence; finite–fault slip model; seismological geodesy; stress transfer and triggering

### Περίληψη

Στις 3 Μαρτίου 2021 ένας ισχυρός σεισμός μεγέθους  $M_w 6.3$  έπληξε την περιοχή της βόρειας Θεσσαλίας προκαλώντας εκτεταμένες βλάβες σε πόλεις και χωριά στην περιοχή όπου έλαβε χώρα η σεισμική δραστηριότητα. Ο σεισμός αυτός ακολουθήθηκε από μεγάλο πλήθος μετασεισμών, οι περισσότεροι από τους οποίους ήταν αισθητοί από τους κατοίκους της περιοχής, και την επόμενη μέρα, την 4 Μαρτίου 2021, από έναν δεύτερο ισχυρό σεισμό μεγέθους  $M_w 6.0$  ο οποίος συνδέεται με την ενεργοποίηση γειτονικού ρήγματος. Οι δύο σεισμοί είναι οι ισχυρότεροι που έγιναν στην περιοχή από το 1941, όταν ένας σεισμός μεγέθους  $M=6.3$  έγινε πολύ κοντά στην πόλη της Λάρισας. Οι κύριοι σεισμοί προκάλεσαν εκτεταμένες ρευστοποιήσεις κυρίως στις όχθες του Τιταρίσιου, παραποτάμου του Πηνειού ποταμού, όπου οι αλλουβιακές αποθέσεις πιθανόν ενίσχυσαν τις εδαφικές κινήσεις. Οι ερευνητικές μας προσπάθειες για την παρακολούθηση και την διερεύνηση της σεισμικής δραστηριότητας, οι οποίες βασίστηκαν στην χρήση των

δεδομένων που λήφθηκαν από τους σταθμούς του Εθνικού Δικτύου Σεισμολογικών Σταθμών καθώς και τους σταθμούς ενός φορητού τοπικού σεισμολογικού δικτύου που εγκαταστάθηκε και άρχισε να παρέχει δεδομένα τρεις μέρες μετά την έναρξη της σεισμικής έξαρσης, οδήγησαν στον καθορισμό και την κατανόηση των γεωμετρικών και κινηματικών ιδιοτήτων των ρηγμάτων που ενεργοποιήθηκαν. Οι μετασεισμοί κατανέμονται σε μία ζώνη μήκους ~40 km, η οποία περιλαμβάνει τις ζώνες διάρρηξης των δύο κύριων σεισμών καθώς και δευτερεύουσες δομές οι οποίες δραστηριοποιήθηκαν αυτό το χρονικό διάστημα, σε συμφωνία με τα αποτελέσματα μοντελοποίησης κυματομορφών και InSAR. Η πρώτη διάρρηξη επεκτάθηκε δικάτευθунτικά, με τη δεύτερη κύρια διάρρηξη να αρχίζει στο βορειοδυτικό της άκρο και να αναπτύσσεται μονοκατευθунτικά βόρεια–βορειοδυτικά. Οι μηχανισμοί γένεσης των δύο κύριων σεισμών δείχνουν σχεδόν καθαρά κανονικές διαρρήξεις, σε συμφωνία με την πλειονότητα των μηχανισμών γένεσης των ισχυρότερων μετασεισμών που καθορίστηκαν στα πλαίσια της εργασίας. Η ισχυρή εδαφική κίνηση του πρώτου κύριου σεισμού υπολογίσθηκε με στοχαστική προσομοίωση μοντέλου ρήγματος πεπερασμένων διαστάσεων. Οι σεισμικές μεταθέσεις που καθορίστηκαν από τις καταγραφές ενός πυκνού δικτύου πέντε μόνιμων σταθμών GPS/GNSS στην περιοχή της Θεσσαλίας, έδειξαν BBD–NNA εφελκυσμό όπως αναμένεται από τις ιδιότητες και τη θέση της κύριας διάρρηξης. Ο υπολογισμός των μεταβολών των τάσεων Coulomb λόγω της σεισμικής ολίσθησης του πρώτου κύριου σεισμού, έδειξε αύξηση των θετικών μεταβολών των στατικών τάσεων κατά 10 bar στην εστία του δεύτερου κύριου σεισμού.

*Λέξεις–κλειδιά:* σεισμική ακολουθία, μοντελοποίηση ρήγματος πεπερασμένων διαστάσεων, σεισμολογική γεωδαισία, μεταφορά τάσεων

## 1. INTRODUCTION

A strong  $M_w$ 6.3 earthquake struck a fault segment ~20 km bounding the west flank of Tyrnavos basin, in Thessalia area, central Greece, on the 3<sup>rd</sup> of March 2021, at 10:16:08.58 UTC (Fig. 1). The main shock is the largest to have struck the area since 1941 when an M6.0 earthquake caused severe damage in the city of Larissa, already bombarded as a battlefield of the Second World War. The epicenter (39.7349°N, 22.1908°E) was about 15 km to the northwest of the city of Larissa, and to the northwest of the Tyrnavos fault, which is the closest fault segment known to be associated with strong earthquakes. This main shock may have initiated onto a fault segment laying to the continuation of Larissa fault and subparallel to Tyrnavos fault segment. The lack of surface ruptures along with the characteristics of the aftershocks distribution, suggest a complex interplay between known active faults with surface expressions and unknown

faults with lack of surface expression. The main shock caused extensive damage and due to its position in both a populated urban area and in a fault population that seems to include several active fault segments, its seismological characteristics are expected to shed more light on the development and physics of normal fault systems.

The 3<sup>rd</sup> of March main shock with  $M_w$ 6.3 was strongly felt throughout most of the central and north Greek mainland, with severe structural damage in the villages very close to its epicenter. Extensive liquefaction was documented mostly close to the banks along the Titarisios tributary, associated with unconsolidated sediments and shoreline deposits. Many tension cracks were observed and documented from an initial field reconnaissance, mainly to sites located on the hanging wall. Numerous aftershocks followed with a plethora of them being felt by the population of the several small towns and villages located both inside and close to the aftershock area. In the first hours several strong aftershocks ( $M \geq 4.0$ ) followed, distributed to an area longer than the causative fault of the 3<sup>rd</sup> of March main shock, beyond to both its edges. The off-fault activity that was northwesterly expanded, was longer and denser and encompassed  $M_5$  aftershocks as well. At the northwest tip of the first main rupture, the second main shock, with  $M_w$ 6.0, nucleated in the next day, on the 4<sup>th</sup> of March, at 18:38:17.46 UTC.

The intense aftershock activity with  $M \geq 4.0$  aftershocks continued for a couple of days and then with smaller magnitude but high aftershock occurrence rate. The teleseismic fault plane solutions (<https://www.globalcmt.org/CMTsearch.html> <http://geophysics.geo.auth.gr/ss/>) indicated that both earthquakes and the largest aftershocks involved normal slip accommodated on northeast dipping faults, as evidenced by the preliminary aftershock spatial distribution. The vigorous aftershock activity was recorded by the Hellenic Unified Seismological Network (HUSN, <https://doi.org/10.7914/SN/HT>) and analyzed in the course of routine analysis at the central Seismological Station of the Aristotle University of Thessaloniki. The aftershocks outline a pattern that favors a model of slip on a northeast dipping fault. However, several aftershocks lie off this trend and could be associated with secondary faults of the local fault population. With these possibilities, we aim to resolve the causative faults associated with this seismic excitation. The importance of resolving the faults activated by the two main shocks lies in their domination on the regional seismic hazard.

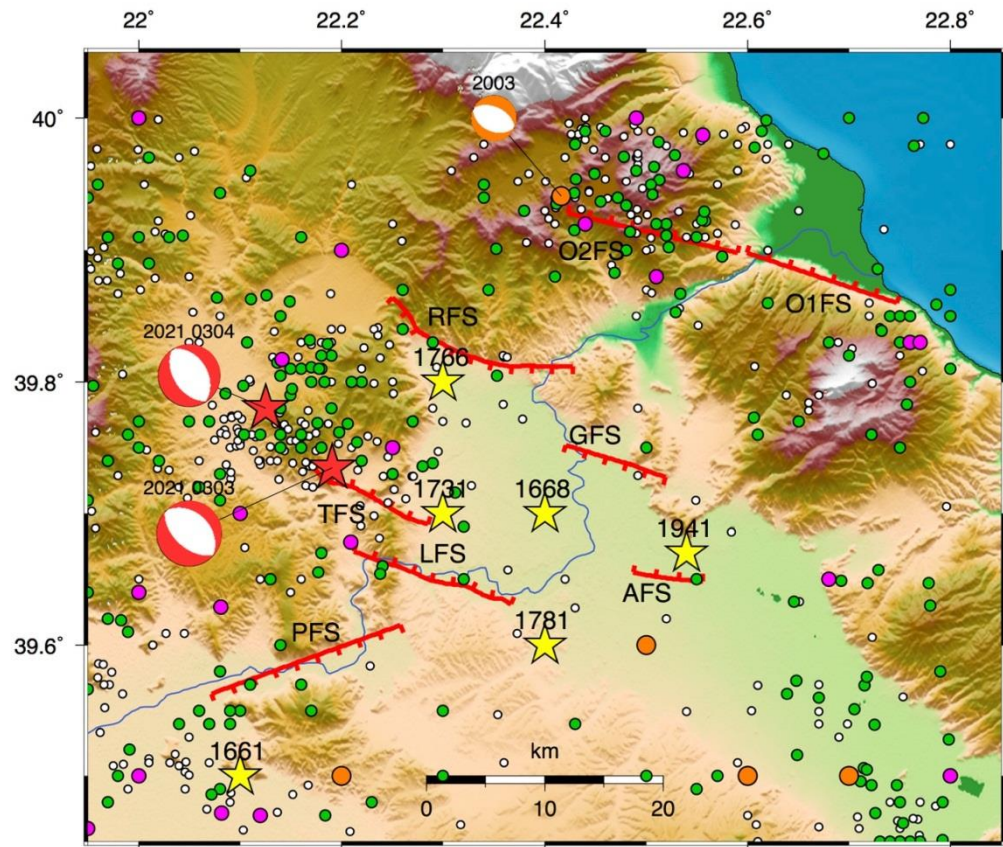


**Fig. 1:** Seismicity and the major fault segments of the Northern Thessaly Fault System. The white, green, magenta, and orange circles depict the earthquakes with magnitudes between  $2.0 \leq M_w < 3.0$  since 1984, the  $3.0 \leq M_w < 4.0$  since 1965, the  $4.0 \leq M_w < 5.0$  since 1951 and the  $5.0 \leq M_w < 6.0$  since 1941, respectively. The epicenters of all known strong earthquakes with  $M_w \geq 6.0$  are shown as yellow stars. The epicenters of the two  $M_w \geq 6.0$  main shocks are shown by the red stars. Their fault plane solutions, as estimated by the Geophysics Department of Aristotle University of Thessaloniki, are shown as equal area lower hemisphere projections with the compression quadrants colored in red. The available fault plane solution of a moderate ( $M_w = 5.2$ ) earthquake, taken from Global Centroid Moment Tensor (GCMT) database is also plotted. The major segments of the Northern Thessaly Fault System, Omolios 1 (O1FS), Omolios 2 (O2FS), Rodia (RFS), Gyrtoni (GFS), Asmaki (AFS), Larisa (LFS), Tyrnavos (TFS) and Pineias (PFS) are represented with the red solid lines and are taken from Caputo and Pavlides (1993) and the 2020 updated version (v3.0) of NOA Faults database (<https://zenodo.org/record/4304613#.YOhI7kxRWEs>).

As far as the regional stress pattern concerns, the area of Thessaly shown in Figure 1, accommodates assorted inherited structures and is currently under the influence of an extensional deformation field. The NE–SW extension (Late Miocene – Early Pleistocene) generated the so-called basin–and–range–like system (Caputo, 1990) consisting of a series of horsts and grabens bordered by NW–SE trending faults. The maximum dimensions of the seismogenic structures rarely exceed 20 – 25 km alike in

the vast majority of the Greek mainland (Goldsworthy et al., 2002), comprising part of the back arc Aegean area. The activated structures constitute the northwest continuation of the Larissa and Tyrnavos faults (Fig. 1), composing a fault zone that bounds from the eastern Thessaly basin to the west. The general N–S extension in the back arc area on E–W normal faults changes to the NE–SW slip vectors on NW–SE striking normal faults, which might be attributed to the relative block rotation, although it is uncertain how the blocks can be identified and their boundaries to be defined. An inherited fault network might also support the strike differentiation. From a palaeoseismological investigation along the Tyrnavos normal fault, striking ESE–WNW, dipping to north and bounding the Tyrnavos basin, Caputo et al. (2004) suggest vertical coseismic displacements of 20–40 cm and possible recurrence time of 2–2.5 ka.

Seismicity in the 2021 rupture zone is relatively low in the instrumental era (Fig. 1) in comparison with other areas in Greece where known active fault networks control and accommodate the current seismic activity. Historical information is not adequate to support reactivation of the fault segments that accommodate the aftershock activity. The current activity provides an excellent opportunity to investigate the details of the faulting and seismotectonic properties. High quality geodetic observations from continuous Global Positioning System (GNSS) network in the study area, as well as Interferometric Synthetic Aperture Radar (InSAR), were collected in the days immediately following the inception of the seismic excitation. The contribution of satellite geodetic observations can provide a critical advantage for the estimation of earthquake magnitude and mechanism, in conjunction with the traditional seismic measurements. These observations recorded ground–to–satellite distances at successive acquisitions that correspond to surface displacements generated by the three major earthquakes of the sequence, including both the coseismic surface displacement field and early postseismic deformation. We process these geodetic observations and discuss their outcome in combination with relocated aftershock spatial distribution, to constrain the activated fault segments. Static stress change calculations show increased Coulomb stress on the second main shock focus as well as to the vast majority of aftershocks.

## **2. GEOTECTONIC SETTING**

### **2.1 Geological and structural characteristics**

The study area consists of crystalline rocks of the Pelagonian zone, which are unconformably overlain by younger lacustrine and fluvial Neogene and Quaternary deposit. The final configuration of the basement is an aggregate of multiple deformation

episodes, both compressional and extensional, which produced brittle and semi-brittle structures of various sense of displacement. The post-orogenic collapse of the Pelagonian zone formed low-angle normal detachment faults, which in turn caused the exhumation of lower tectonostratigraphic units and the formation of characteristic tectonic windows.

This extensional tectonic deformation went on during the neotectonic period, with two main phases:

1. During Upper Miocene – Pliocene, the extensional stress field had a NE–SW direction, causing the deformation of large normal fault zones of NW–SE strike. These fault zones formed long, complex grabens of the same strike throughout central and northern Greece. In the area of Larisa plain, these zones mark its eastern and western margins.
2. During the Quaternary, the extension direction switched slightly to NNE–SSW, causing the formation of younger faults of WNW–ESE strike. These faults define the northern margin of Larisa plain, and they can be classified into two main groups:
  - a. Faults dipping to SSW. These are mainly the Rodia and Gyrtoni faults, and they are generally delineating the boundary between the marginal formations to the North and the Larisa plain to the South.
  - b. Faults dipping to N and NNW. Those faults (Tyrnavos, Larisa and Asmaki) are antithetic to the ones of the first group. They do not have as intense morphotectonic signature, neither their cumulative deformation is as large. They are considered secondary structures in relation to the ones marking the northern Larisa plain boundary; however, they are of particular interest as they are considered active and are closer to the large population centers of the area, increasing thus the inherent seismic hazard.

Paleoseismological studies in the area (Caputo et al., 2004, 2006; Tsodoulos et al., 2016a, b) showed that there are several faults of low slip rate (up to 0.2 mm/yr) and surface displacement of *ca.*20-40 cm per event. Despite being “slow” faults (i.e. associated with long recurrence interval), they pose a significant risk due to the fact that they can produce events of up to  $M \sim 6.5$ , based on their geological, geometrical and paleoseismological characteristics.

## 2.2 Seismic faults and surface effects

Based on field work and the available seismological information (from <http://geophysics.geo.auth.ss/>; doi:10.7914/SN/HT), the causative seismic fault belongs to a low-angle normal fault zone, which is considered blind, as it does not reach the surface (Pavlidis et al., 2021). Its dip angle of 36° is in good agreement with the attitudes of bedrock detachment faults that were caused by the collapse of the Pelagonian orogene (Kilias et al., 2010, 2016). This is of particular importance, as it is a non typical behavior of an older, inherited alpine structure with no surface expression. The earthquake sequence of March 2021 formed various secondary effects, which are shown in Figure 2. They can generally be classified into the following groups (Ganas et al., 2021; Pavlidis et al., 2021; Valkaniotis et al., 2021):

1. **Liquefaction:** they were mainly formed in the area close to the northern banks of Pinios river, near Piniada village, while a smaller liquefied area was formed near Vlachogianni village in the alluvial plain of Titarisios river. In both areas, the liquefied material consists of fine-grained alluvial deposits, while in the main liquefied area of Piniada the vast majority of liquefaction structures was concentrated in paleobeds of Pinios River. They were particularly susceptible to liquefaction, because they were filled with fine-grained sediments after their abandonment, and they are mechanically weaker zones.
2. **Surface ruptures.** Surface ruptures were localized, generally of short length and they are interpreted as secondary structures. Although small ruptures were scattered throughout the area (interpreted as local effects of gravitational slope failure), significant linear structures were observed in mainly two sites:
  - 2.1. SE of Mesochori. They are small-scale (~1 km) ruptures with displacement of a few cm to the SW and occasional heave of 2–3 cm. They coincide with a morphotectonic NW–SE directed lineament, which is most probably associated with a normal fault that delineates Titarisios valley. Based on seismological data (epicenter location, focal mechanism etc.) it is considered that movement on this fault was triggered by the activation of the main fault. Therefore, it is considered a secondary deformation on a sympathetic supra-detachment fault.
  - 2.2. Zarkos – Megalo Eleftherochori. They consist of a set of spaced open ruptures of NW–SE strike, with no significant vertical displacement. Their position coincides with the extrapolated projection of the top of the main blind low-angle fault. These fractures are

considered secondary, although they are characteristic of the geological expression of the seismic fault.

3. **Rockfalls.** Rockfalls and slope failures were observed throughout the affected area (i.e. Damasi, Vlachogianni, Grizano, Damasouli, etc.), which are not associated with the activation of any of the faults, but their distribution is rather random and dependent only on the local geotechnical and morphological conditions.

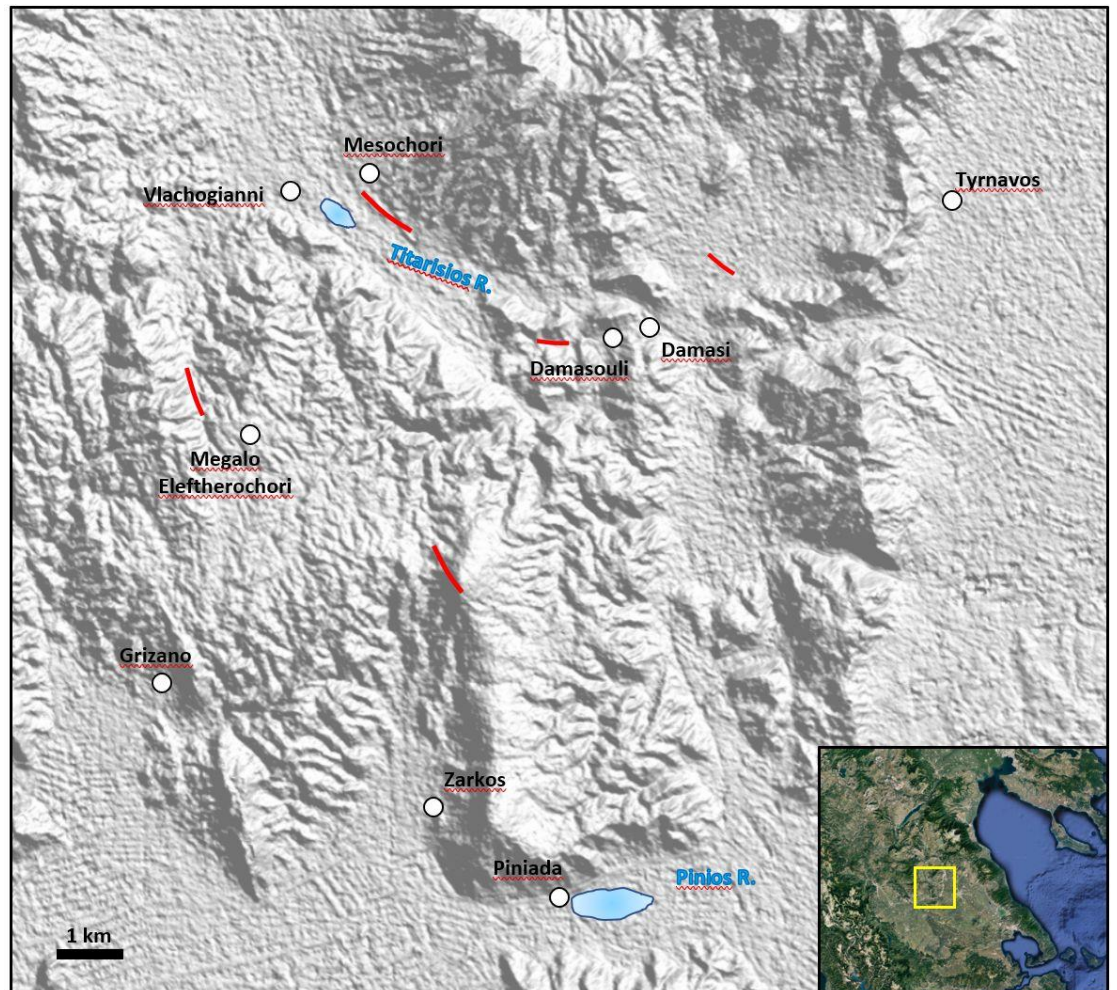


**Fig. 2:** Location map of the study area, the secondary effects and the sites mentioned in the text. Red lines: surface ruptures. Blue areas: liquefied areas. Inset shows the location of the area in central Greece.

### 3. THE AFTERSHOCK SEQUENCE

#### 3.1 Aftershock data

To accomplish a detailed investigation of the aftershock pattern and the evolution of the aftershock sequence, we analyzed seismic data recorded between 3 of March and

03 of April 2021, by the stations of both the Hellenic Unified Seismological Network (HUSN) and the portable temporary network, and retrieved in the Seismological Station of the Geophysics Department of the Aristotle University of Thessaloniki (<https://doi.org/10.7914/SN/HT>), for manual phase picking and initial location. Stations up to the distance of ~150 km were selected for the relocation improvement, and are shown in Figure 3 as inverted red triangles along with the epicenters of the two main shocks, which are depicted by stars. A portable seismic network of seven (7) stations was installed in the epicentral area to enhance seismicity detectability and location improvement, also shown in Figure 3 and in larger scale in the inset map. The inverted yellow triangles depict the sites of the stations the recordings of which were used for the moment tensor inversion.

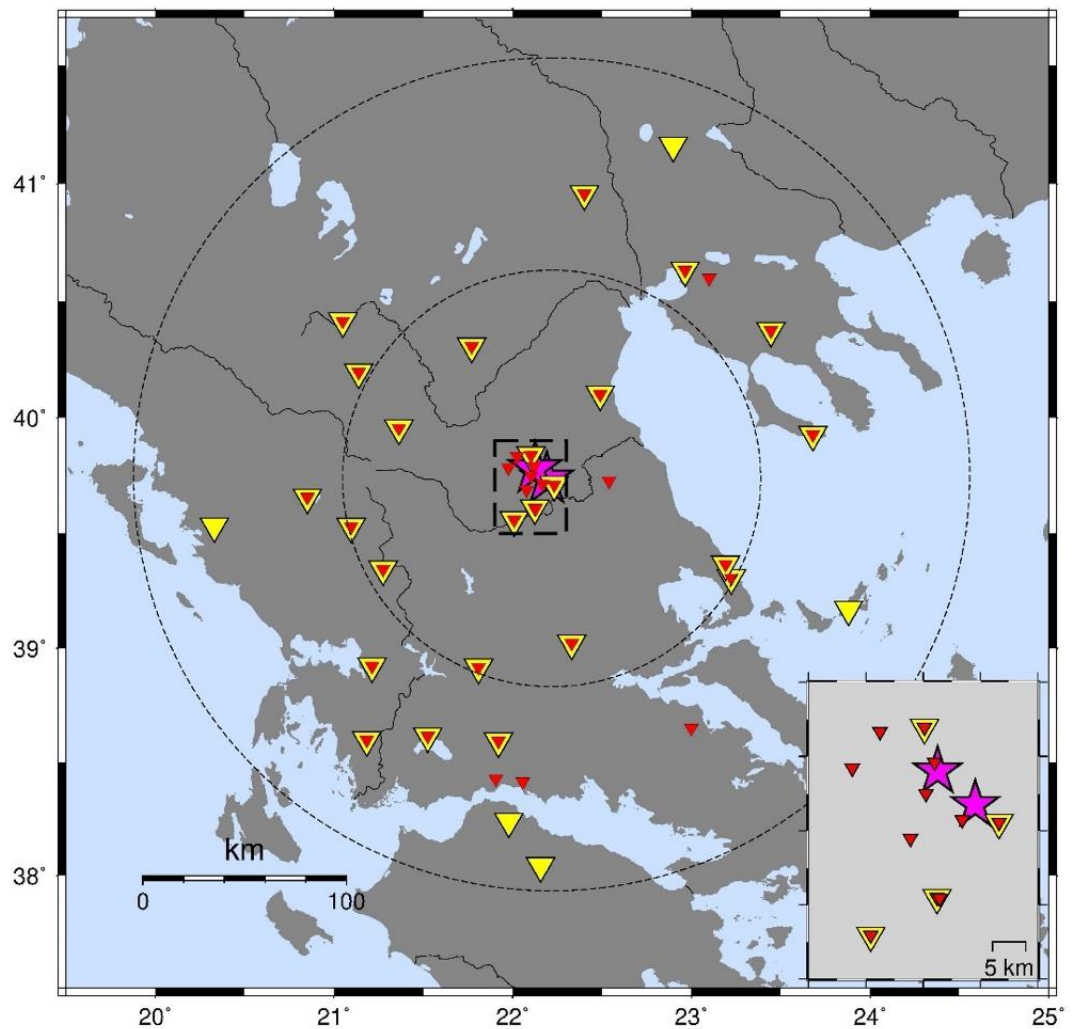


**Fig. 3:** Stations from the regional Hellenic Unified Seismological Network (HUSN) the recordings of which were used in earthquake relocation (red inverted triangles) and moment tensor inversions (yellow inverted triangles). Inset map shows the stations of the dense portable network. The magenta stars depict the two main shocks epicenters.

### 3.2 Aftershock location

A first improved location was achieved by setting a minimum number of eight (8) arrival times for each earthquake and calculating a  $V_p/V_s$  ratio that was found equal to 1.76. The velocity model given in Table 1 was defined using the *Veltest* software (Kissling et al., 1994) and earthquakes that were recorder by the local network. The lateral inhomogeneities were considered by calculating and incorporating in the location process, time corrections for each seismological station.

Using the program Hypoinverse (Klein, 2002), we calculated mean  $1\sigma$  error for absolute horizontal error  $0.68 \pm 1.02$  km and vertical error  $1.37 \pm 2.01$  km. We applied then waveform relocation process, which provided relative errors an order of magnitude smaller than the absolute errors. The relocation was accomplished with the HypoDD software (Waldhauser and Ellsworth, 2000) using catalog differential times to obtain more precise origin times for waveform preparation for the next step. Then, we used cross-correlation differential times (Schaff et al., 2004) along with catalog differential times performed by the HypoDD computer program (Waldhauser and Ellsworth, 2000) and cross correlation differential times (Schaff and Waldhauser, 2005).

**Table 1.** P-wave velocity model for the location of the sequence.

Depth (km)	$V_p$ (km/s)
0.0–2.0	5.35
2.0–2.5	5.41
2.5–6.0	5.73
6.0–7.0	5.97
7.0–8.0	6.04
8.0–9.0	6.10
9.0–13.0	6.15
13.0–14.0	6.24
14.0–15.0	6.32
15.0–29.0	6.46
29.0–34.0	7.65
$\geq 34.0$	7.8

### 3.3 Aftershock fault plane solutions

Moment tensors were estimated for twenty four (24) of the strongest aftershocks while for the two mainshocks we adopted the solutions of GCMT (<https://www.globalcmt.org/CMTsearch.html>) and GFZ (<https://geofon.gfz-potsdam.de/eqinfo/form.php>) solutions, respectively. The moment tensor inversions for the aftershocks were performed with the Grond software (Heimann et al. 2018) which operates within the Pyrocko toolbox (Heimann et al. 2017), using recordings from the regional seismological stations (shown in Figure 3 with yellow triangles).

The waveforms used for the inversions were filtered in the 0.05–0.1 Hz frequency band and applying a taper fall-off factor of 1.1 [ $f_{min}/factor$ ,  $f_{max}*factor$ ]. The Green's functions were estimated by the QSEIS program (Wang, 1999) operated through the Pyrocko software, and using the crustal model of Table 1. The inversion was performed for a deviatoric moment tensor in the time domain assuming a point source model. A Bayesian bootstrap-based probabilistic procedure was employed for 25000 iterations, aiming to minimize the L2-norm misfit between observed and calculated waveforms with 200 parallel bootstrap chains for estimating the uncertainties.

### 3.4 Aftershock distribution

The aftershock seismicity catalog extends for 32 days and comprises 1476 aftershocks, which have been relocated with high accuracy. This provides the tool of detailing the properties of the two main ruptures and the secondary faults of the local fault network that have been possibly triggered by the slip redistribution and stress transfer mainly due to the coseismic slip of the two largest ( $M_w$ 6.3 & 6.0) ruptures. The spatial aftershock distribution (Fig. 4) defines a narrow strip exceeding in length the 50 km and aligned in a general NW–SE direction.

The epicentral alignment agrees well with the normal faulting type of the two main shocks, the fault length is however appreciably larger than expected from their magnitudes, estimated to be of the order of 20 km each one from empirical relations for normal faults by both Wells and Coppersmith (1994) and Papazachos et al. (2004).

**Table 2.** Information on the fault plane solutions determined in this study along with the ones adopted from other Institutions, referred in the last column, for earthquakes occurred between 03/03/2021 to 21/03/2021.

N	Date	Time	Lat (°)	Long (°)	h (km)	M <sub>w</sub>	M <sub>o</sub> (Nm)	Strike (°)	Dip (°)	Rake (°)	Ref
1	2021/03/03	10:16:08.58	39.7349	22.1908	9.5	<b>6.3</b>	2.20e+18	314	36	-88	AUTH
2	2021/03/03	11:19:02.10	39.7287	22.2102	7.98	4.0	8.99e+14	283	29	-153	This study
3	2021/03/03	11:45:45.70	39.6909	22.2025	8.29	5.2	6.56e+16	310	47	-74	This study
4	2021/03/03	18:24:08.72	39.7225	22.0813	10.0	5.1	5.83e+16	319	38	-62	This study
5	2021/03/04	02:43:38.38	39.7111	22.2235	9.6	4.2	2.04e+15	331	54	-57	This study
6	2021/03/04	05:10:20.54	39.6198	22.2651	4.4	3.7	3.47e+14	312	41	-94	This study
7	2021/03/04	09:36:15.70	39.7803	22.1135	7.9	4.5	6.46e+15	132	53	-81	This study
8	2021/03/04	18:38:17.46	39.7799	22.1252	12.00	<b>6.0</b>	1.30e+18	329	41	-88	GFZ
9	2021/03/04	19:23:51.18	39.8224	21.9313	7.86	5.1	5.84e+16	287	30	-91	This study
10	2021/03/05	19:43:23.72	39.7601	21.9722	19.00	3.9	7.68e+14	282	57	-87	This study
11	2021/03/06	16:36:18.13	39.6709	22.2383	2.63	4.1	1.44e+15	257	35	168	This study
12	2021/03/06	19:47:40.21	39.8294	22.0658	2.47	4.2	2.11e+15	302	39	-105	This study
13	2021/03/08	18:00:45.09	39.5990	22.2724	1.85	4.0	1.17e+15	309	38	-112	This study
14	2021/03/08	18:07:03.14	39.6062	22.2600	2.45	3.9	7.47e+14	312	40	-105	This study
15	2021/03/08	18:34:20.77	39.7099	22.1062	10.88	4.0	9.63e+14	237	88	159	This study
16	2021/03/09	04:30:32.86	39.8735	21.9836	11.39	3.8	5.48e+14	266	47	-109	This study
17	2021/03/11	14:19:40.41	39.7788	22.0791	5.38	4.3	3.03e+15	267	49	-105	This study
18	2021/03/12	12:57:50.14	39.8281	22.0150	3.34	5.5	2.25e+17	286	53	-92	This study
19	2021/03/12	14:11:35.99	39.8198	22.0421	2.78	4.0	1.16e+15	311	40	-100	This study
20	2021/03/12	15:00:20.09	39.8186	22.0196	5.75	4.1	1.62e+15	286	47	-80	This study
21	2021/03/13	15:09:12.83	39.8038	22.0045	4.48	4.3	3.29e+15	278	43	-85	This study
22	2021/03/15	15:43:36.39	39.7500	22.1209	5.54	4.5	6.21e+15	349	37	-44	This study
23	2021/03/17	03:51:32.50	39.6287	22.2657	4.70	4.0	9.57e+14	274	60	-110	This study
24	2021/03/19	15:50:17.16	39.8141	22.0314	6.20	4.0	9.88e+14	297	61	-101	This study
25	2021/03/19	20:39:19.56	39.7849	22.1073	7.90	3.8	5.86e+14	311	34	-109	This study
26	2021/03/21	17:15:54.00	39.7722	22.1036	8.9	4.1	1.59e+15	321	37	-52	This study

It must be noticed here that these two scaling relations are neither the only ones nor the most reliable, among others. They have been used nevertheless in a plethora of studies and are used here for the sake of comparison. The highly accurate hypocentral relocation gears the decomposition of the aftershock seismicity into components associated with distinct fault segments. Since the aftershock activity covers a larger area than expected from the causative faults of the two main shocks, the identification is seeking of both the two main ruptures dimensions and position and the “off fault” activity, connected with the activated secondary faults of the local fault network. Fault plane solutions imply almost pure normal faulting onto planes striking NW–SE and dipping to the northeast (Table 2 and Fig. 4). This strike is compatible with the observed surface expressions as described in the previous section. The fault plane solutions of the two main shocks as have been determined by other agencies also show almost pure normal faulting with comparable strike and dip angles (Table 2).

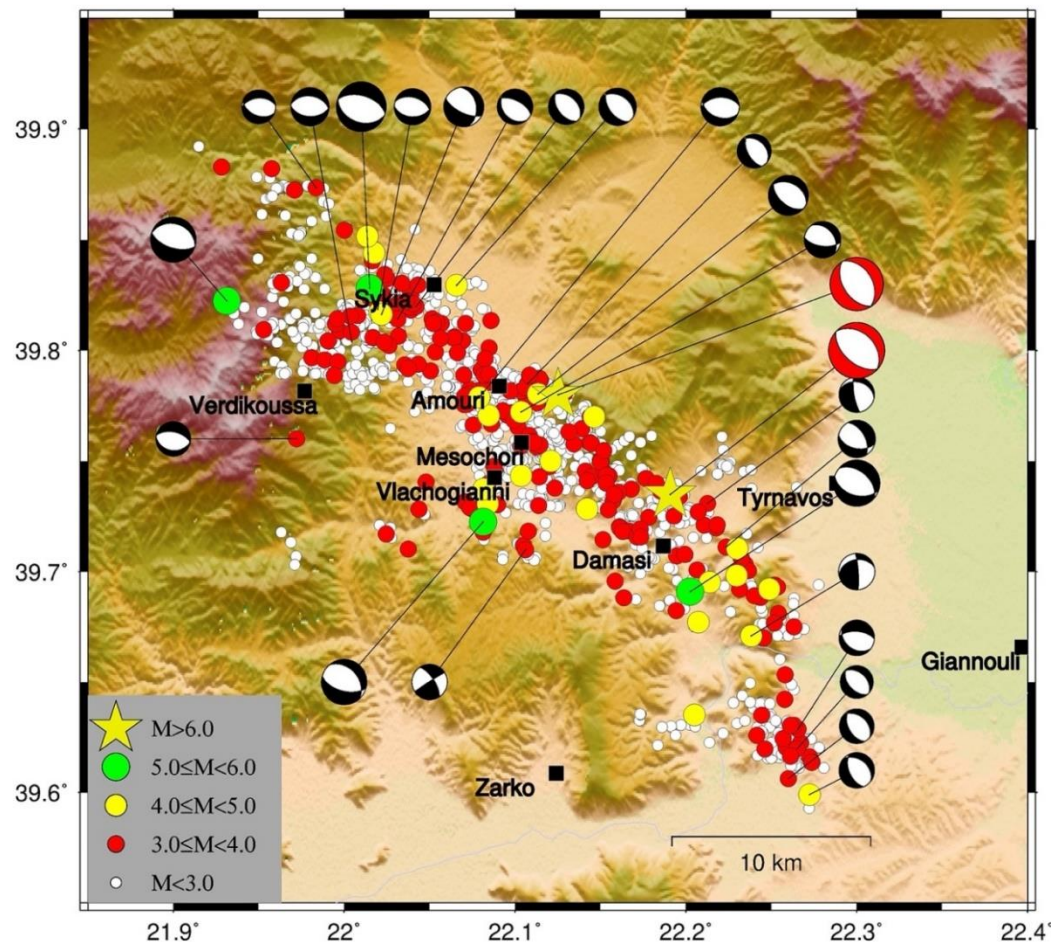


**Fig. 4:** Epicenters of the relocated aftershocks of the sequence for the period March 3–April 3, 2021, shown by circles with different color and size, according to their magnitude range as shown in the inset. Fault plane solutions are shown as lower hemisphere equal area projections, with the compression quadrants colored, red for the two main shocks and black for all aftershocks.

The largest ( $M_w \geq 5.0$ ) aftershocks (green circles in Fig. 4) occurred close in time with the two main shocks but outside the main rupture areas, as detailed below in the text and shown in Figures 5 and 6, created their own aftershocks and revealing secondary fault segments of the local fault network. The northernmost part of the epicentral distribution, encompasses two strong ( $M_w \geq 5.0$ ) aftershocks, several moderate ( $M_w \geq 4.0$ ) ones, and dense minor magnitude seismicity forming a remarkable seismicity cloud and implying the activation of several minor fault segments, either subparallel or antithetic, an observation that needs further analysis. The southeastern distinctive cluster shown in Figure 4 is formed after a spatial gap in the activity, is closely connected in time with the first main shock, with an epicentral alignment almost at the same strike, but stepping by a few kilometers.

The first main shock relocated epicenter lies to the northwest of the Tyrnavos normal fault, revealing an adjacent activated fault segment that cannot be associated with any known earthquake. The abundant aftershocks that follow in the first hours were adequate to shed light on the causative fault geometrical parameters. Figure 5a shows the aftershock activity in the first six hours after the occurrence of the March 3, 2021, main shock. This aftershock zone outlines a ~17 km long zone, with a NW–SE orientation ( $\sim 315^\circ$ ), in full agreement with the strike of the focal mechanism determined by GCMT (Table 2) and the aftershocks distributed either side of the main shock epicenter. The stronger ( $M \geq 4.0$ ) aftershocks lie between the main shock epicenter (yellow star) and the southern fault edge, where the  $M_w = 5.2$  aftershock (green circle) was also nucleated. The strike–normal cross section (Fig. 5b) indicates that the depth range of the overall seismicity was from ~4 to ~12 km. The largest aftershock occurred at the down–dip end of the main rupture, slightly dipper than the main shock. The main shock nucleated at the lower part of the seismogenic layer, consistently with the aftershocks alignment in depth that presents a dip angle of  $38^\circ$ , in the least squares' sense, again in full agreement with the fault plane solution.

The duration of six hours was selected because for longer periods there is a shift of the seismicity to the NW in the area where the second main shock with  $M = 6.0$  occurred in the next day. This activity could be foreshock activity of the second strong earthquake and not aftershocks of the main shock. In addition, there is evidence that the magnitude  $M = 5.1$  earthquake which occurred in less than one hour after the main shock (Fig. 6, green symbol west of the main shock). Most of the first six hours seismicity defines the rupture dimensions (blue rectangle in the map view projection in Figure 6a), a length of 15 km and a width of 8 km, as they are given in detail in Table 3. In the cross section (Fig. 6b), we observe a noticeable fit of a dip at  $46^\circ$ , a typical dip angle for normal faults

in continental areas (Abers et al., 1997), and in agreement with the centroid moment tensor solution listed in Table 2.

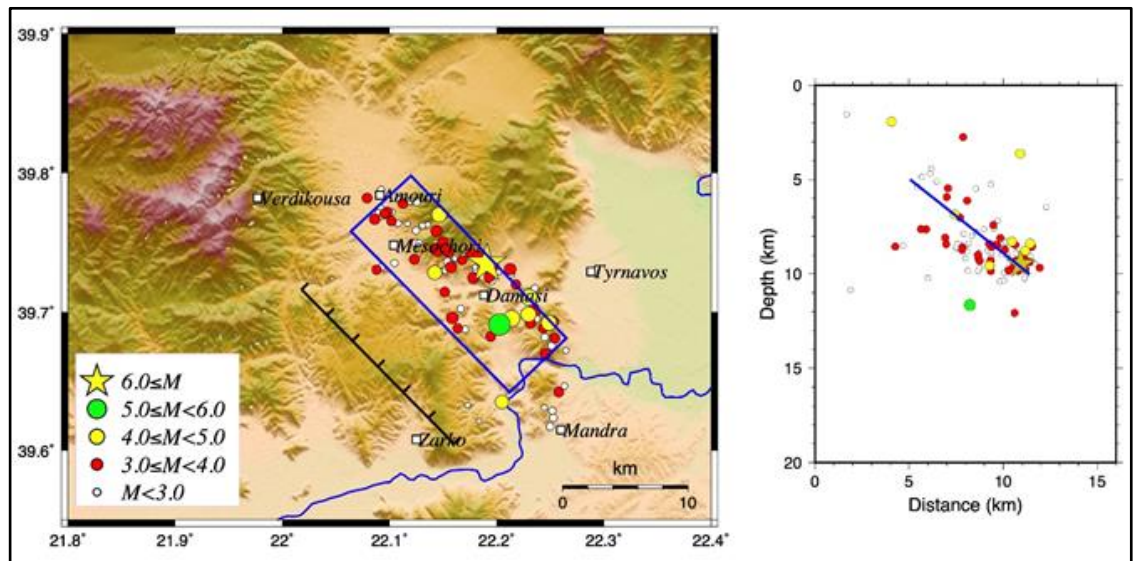


**Fig. 5:** (a) Relief and aftershock location map for six hours after the occurrence of the first main shock (3 March 2021). The blue rectangle indicates the surface projection of the rupture area. (b) Strike–normal cross section with the seismicity shown in (a). The blue line approximates the fault dip. Symbols are as in Figure 4.

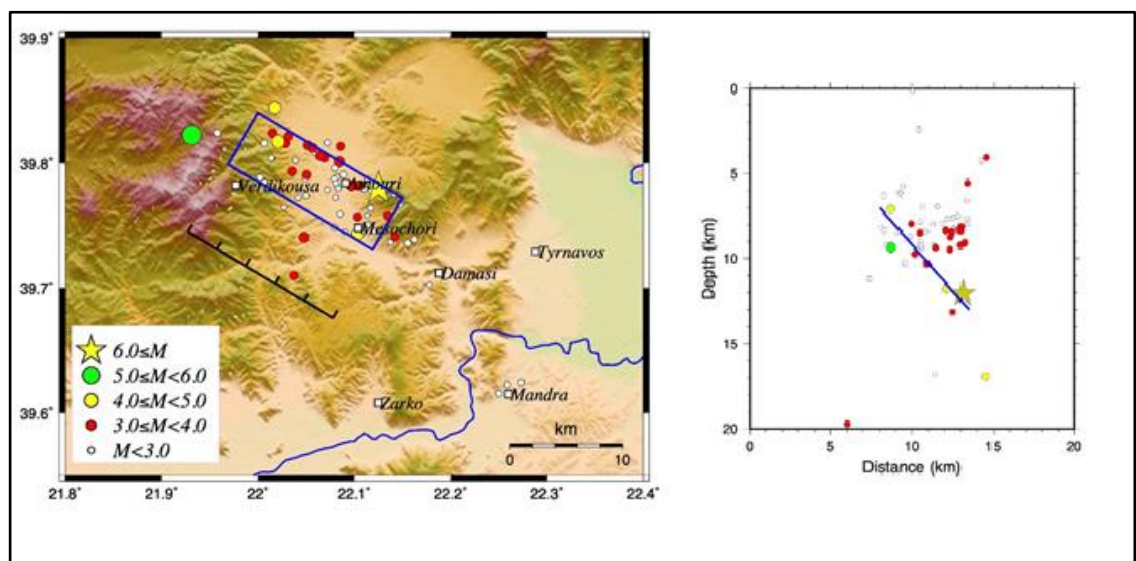


**Fig. 6:** (a) Same as in Figure 5a for six hours after the occurrence of the second main shock (4 March 2021). (b) Strike–normal cross section with the seismicity shown in (a). The blue line approximates the fault dip. Symbols are as in Figure 4.

**Table 3.** Faulting parameters of the two causative main fault segments as derived from the relocated aftershocks 3D spatial distribution. Mean slip is calculated from the seismic moment and the fault dimensions,  $u = M_0 / \mu S$  (considering rigidity  $\mu = 3.3 \cdot 10^{11}$  dyn cm<sup>-2</sup>).

Main shock	1 <sup>st</sup> 2021-03-03	2 <sup>nd</sup> 2021-03-04
Origin time	10:16:08.6	18:38:17.5
Epicenter	39.7349/22.1908	39.7799/22.1252
Depth (km)	9.5	12.0
M <sub>w</sub>	6.3	6.0
M <sub>o</sub>	3.14*10 <sup>25</sup> dyn*cm	1.12*10 <sup>25</sup> dyn*cm
Strike /dip (from aftershock distribution)	315°/38°	300°/46°
Length and width from aftershocks	17 km / 8 km	15 km / 8 km
Mean slip	70 cm	28.3 cm

### 3.5 Temporal evolution of the sequence

The spatial and temporal characteristics of an aftershock sequence are a manifestation of internal crustal dynamics involving the redistribution of stress and displacement fields. To seek for these characteristics the spatio-temporal evolution of the sequence is investigated (Fig. 7), by detailing the pattern of the aftershock locations over time. The duration of the plot equals to 12 days, starting from the first main shock (3 March 2021, M<sub>w</sub>6.3) occurrence. The distances are measured along an SE–NW trending axis, running parallel to the epicentral alignment shown in Figure 3. Three ellipses are drawn to delimit three distinctive spatiotemporal clusters. The southern ellipse encloses a dense cluster beyond the southern edge of the fault segment associated with the first main shock, commenced synchronously with the beginning of the seismic excitation, and located to the south of Pinios River. The first main shock is associated with a fault segment 17 km long, defined with the first hours' aftershocks that are enclosed in the second ellipse. All the M<sub>≥</sub>4.0 aftershocks are included in this set, with their spatial distribution implying bilateral rupture propagation. Beyond to both edges of the main fault two M<sub>≥</sub>5.0 aftershocks (green circles in Figure 7) occurred in the first day, implying crack tip stress concentration because of the coseismic slip.

Northern more, M<sub>≥</sub>4.0 aftershocks (yellow circles in Figure 7) appear densely concentrated until the occurrence of the second main shock in the evening of the next day with M<sub>w</sub>=6.0 (the second star in Figure 7). Thereafter, aftershocks concentrate to the northwest of the second main shock epicenter, covering a zone of 15 km in length (third ellipse in Figure 7), implying unilateral rupture. To the prolongation of this rupture and in less than one hour afterwards, an M=5.1 aftershock took place, around

which the activity is rather sparse. The fourth and last strong ( $M \geq 5.0$ ) aftershock took place at the northwestern part of the activated area where the activity was rather hypotonic, on 12 March, with  $M_w=5.5$  (last green circle in Figure 7). Its occurrence, however, rejuvenated the seismicity, with a dense spatiotemporal cluster of M3 aftershocks (red circles close to its position in the plot of Figure 7).

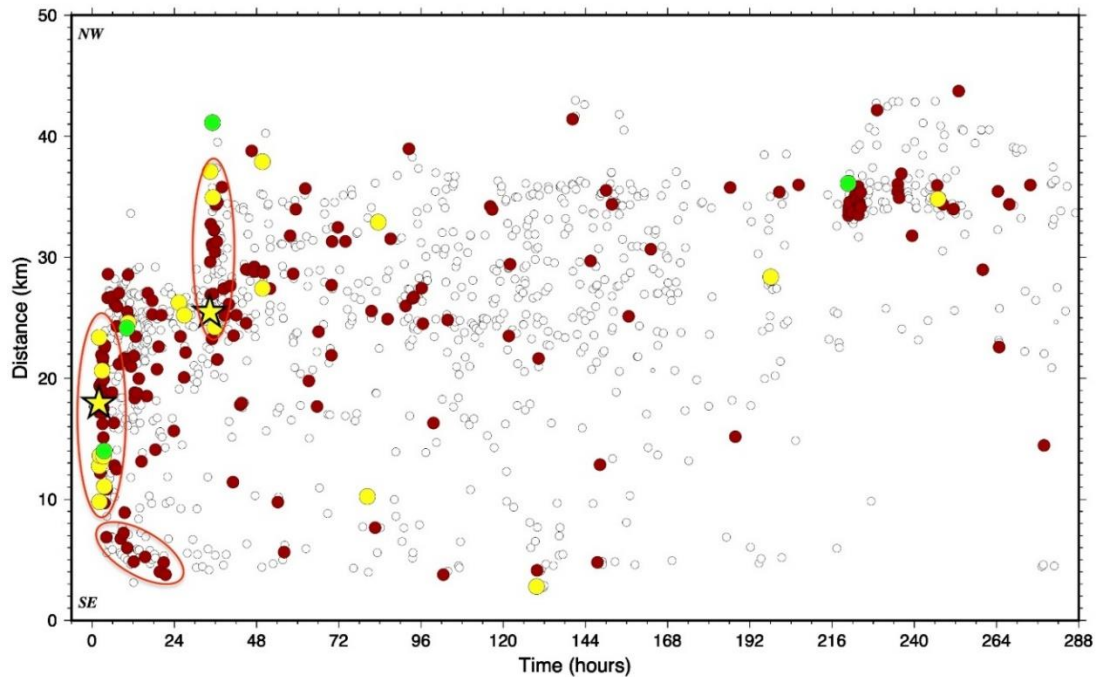


**Fig. 7:** Space–time plot during the first twelve days of the 2021 Tyrnavos seismic sequence. The ellipses define distinctive seismicity clustering for the two main shock and a southern activated minor fault segment. Symbols are as in Figure 4.

#### 4. FINITE–FAULT SLIP INVERSIONS

We used inversion of regionally recorded seismic waveforms to resolve the spatial and temporal distribution of the rupture slip of the two main shocks, which occurred on 3 and 4 March 2021, respectively. Slip models describe the time history of the rupture kinematics with no specific reference to the causative stresses. Good knowledge of the detailed rupture process is essential for realistic simulations of strong ground motion, especially in the case of a complex source.

##### 4.1 Data and methods

The seismic data consist of three–component waveforms recorded by broad band seismometers at stations located at regional distances. The location of the earthquakes is quite optimum within the seismic networks of Greece, and a good coverage in all

azimuths was attained (Fig. 8a). Preprocessing of the initial waveforms includes removal of trend, downsampling to 1 sps, correction for the instrument response, and integration to displacement. Synthetic data were calculated using Green's functions, which are the displacements at the used stations due to an impulsive force and connect data and model parameters. We calculated theoretical Green's functions calculated by a frequency–wavenumber integration method, adopting the 1-D velocity profile (Fig. 8b) of Novotny et al. (2001). The velocity model has proven to be effective in modeling regional wave propagation for earthquakes in Greece. Both the data and theoretical Green's functions were bandpass filtered using an acausal Butterworth filter with corners at 0.2 Hz and 0.08 Hz.

To invert the data we adopt a nonnegative, least-squares inversion method with simultaneous smoothing and damping, as developed by Dreger and Kaverina (2000) and Kaverina et al. (2002). This method inverts for fault slip distributed over a grid of point sources that are triggered according to the passage of a circular rupture front. If required by the data, distortions from the constant rupture velocity and variations in the rise time can be accomplished by using the multiple–time–window technique of Hartzell and Heaton (1983). This method allows each point source to rupture in any of the time windows considered after the initial rupture trigger time. Smoothing, slip positivity, and a scalar moment minimization constraint is applied in all the inversions (see also Benetatos et al., 2007). The amount of smoothing can affect the peak value of slip but does not obscure the average distribution of slip.

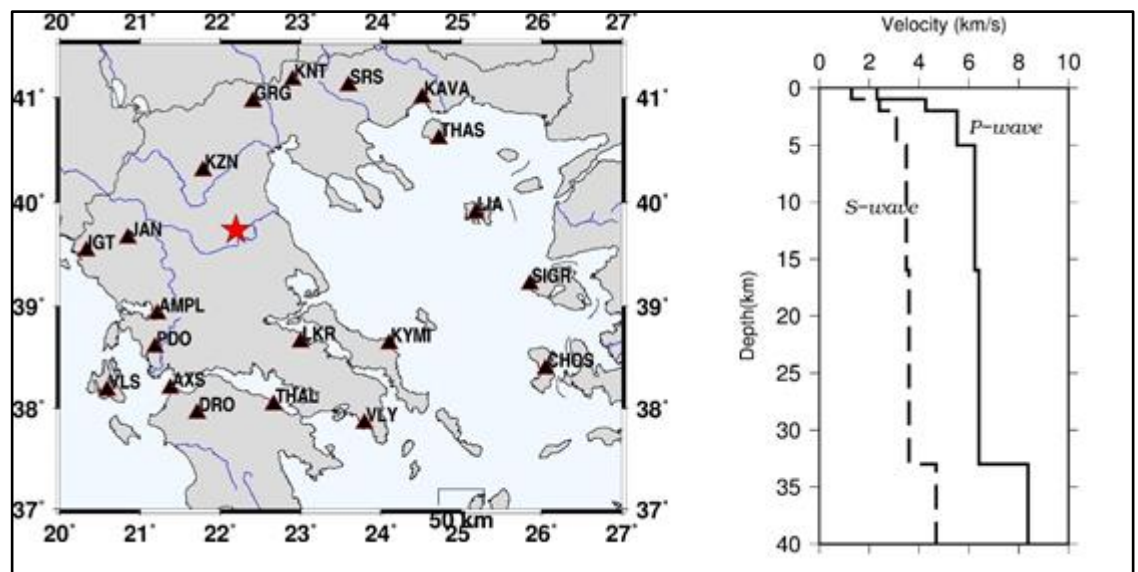


**Fig. 8:** (a) Broad-band stations (triangles) whose waveforms were used in the inversions. (b) 1-D velocity model adopted to calculate Green's functions at regional distances, to perform the low–frequency inversions.

## 4.2 Model parameterization

To setup the fault models for the inversions, the initial fault models have at least doubled dimensions of those expected from empirical relations, for the size of the earthquakes examined, in order to corroborate unilateral rupture propagation and allow the slip to go to its preferable location. The dislocation rise time in each case is adopted using appropriate scaling relations from Somerville et al (1999). The rupture speed is grid searched and values that fit the data and provide reasonable spatial distribution of the slip are finally chosen. In both cases, the hypocenter parameters are the herein relocated ones.

## 4.3 Preferred Slip Models

*Mainshock of 3 March 2021:* We adopted the geometry of the fault plane with strike, dip, and rake angles, equal to  $314^{\circ}/36^{\circ}/-88^{\circ}$ , respectively, as calculated by time–domain moment tensor inversion and reported to EMSC (AUTH solution). The initial fault of  $35 \text{ km} \times 18 \text{ km}$  in length and width, respectively, was discretized in  $1 \text{ km} \times 1 \text{ km}$ , resulting in 630 subfaults where slip is determined in the model. Given the assumed depth of the hypocenter, of 9.5 km, the dip ( $36^{\circ}$ ) of the fault, and the subfault dimension, the top of the fault system is at 2.44 km depth (Table 1). The dislocation rise time is characterized by an isosceles triangle with a duration of 0.8s.

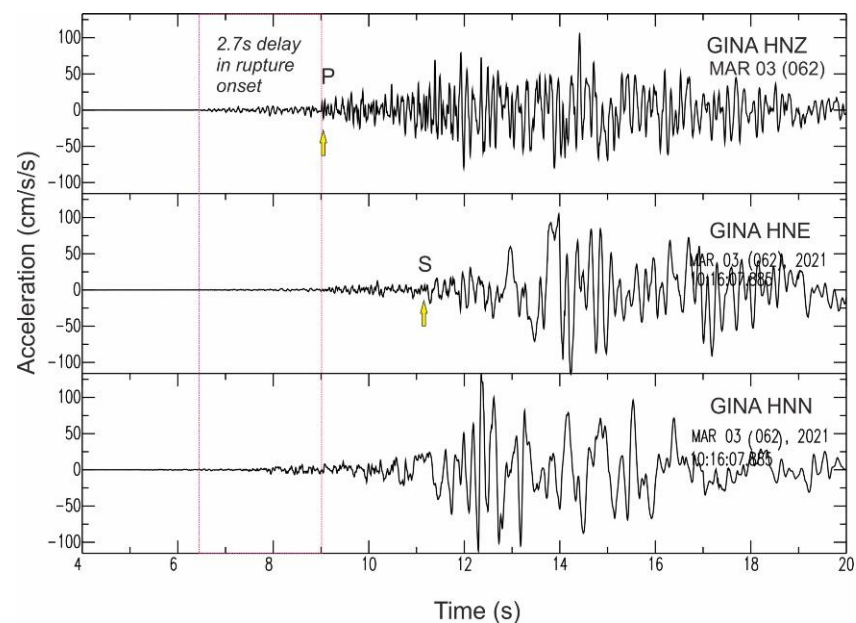


**Fig. 9:** Three–component acceleration recordings of the mainshock at station GINA (Giannouli in Fig. 4), located  $\sim 17 \text{ km}$  away from the epicenter. A delay of  $\sim 2.7 \text{ s}$  is visible in rupture onset, which is corroborated in the finite-fault inversions by a rather slow rupture speed required by the data.

A series of initial inversions were performed to examine the stability of the location of the major slip patches. We started with a single fault that ruptures within a single time window. Then we applied the method of multiple time windows, again for a single fault segment that ruptures within four time–windows. Rupture speed cannot be satisfactorily resolved. A range of rupture speeds was tested, and for the single time window case, a slow rupture speed (in the range 1.2 km/s to 1.8 km/s) provides better fit to the data. This slow rupture speed was also found to corroborate the  $\sim 2.7$ s delay in the rupture onset as observed in the accelerograms from the closest stations (Fig. 9). For the case of multiple time-windows a rupture speed of 2.5 km/s which is 74% of the  $V_s$  velocity at the source depth, provides the same slip distribution and slightly improves the fit.

Figure 10 summarizes the slip model for the main shock. Slip is mainly confined in one major patch located updip from the hypocenter and towards ESE. The centroid is 7.5 km away from the epicenter corroborating the 6.1 s difference between the centroid time and the hypocenter time as reported by GCMT, and the rupture speed considered.

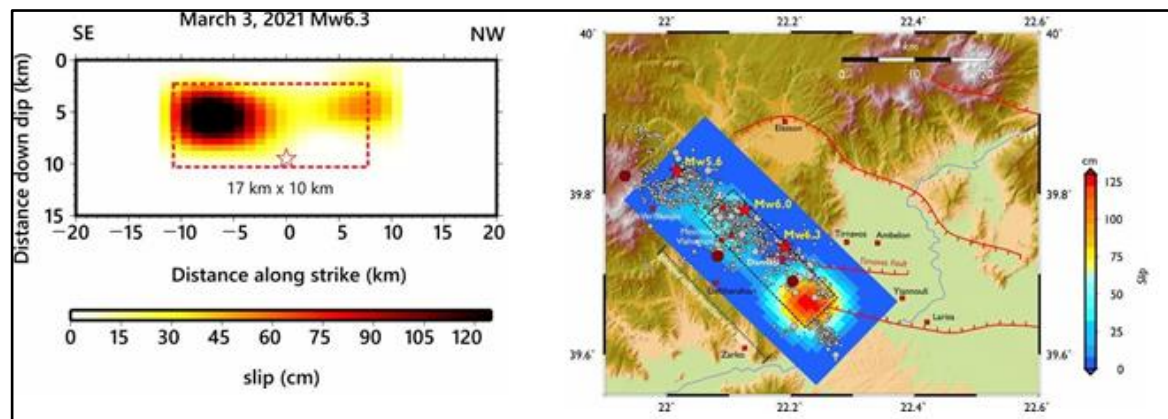


**Fig. 10:** Left: Spatial distribution of slip for the mainshock, along  $314^\circ$  fault strike direction. Slip is confined in a major slip patch (dashed rectangle) located 7.5 km SE of the hypocenter (asterisk). The rupture initiated at the bottom of the fault and propagated updip. Right: Projection to the surface of the slip distribution alongside the relocated aftershocks (circles). The dashed rectangle denotes the fault dimensions associated with the main shock, and the dashed line denotes the inferred surface projection of the fault. For this model parameterization the resolved seismic moment is  $3.82 \cdot 10^{25}$  dyn-cm, resulting in  $M_w=6.32$  and the average slip value is 70 cm for a shear modulus of  $3.2 \cdot 10^{11}$  dyn/cm<sup>2</sup>.

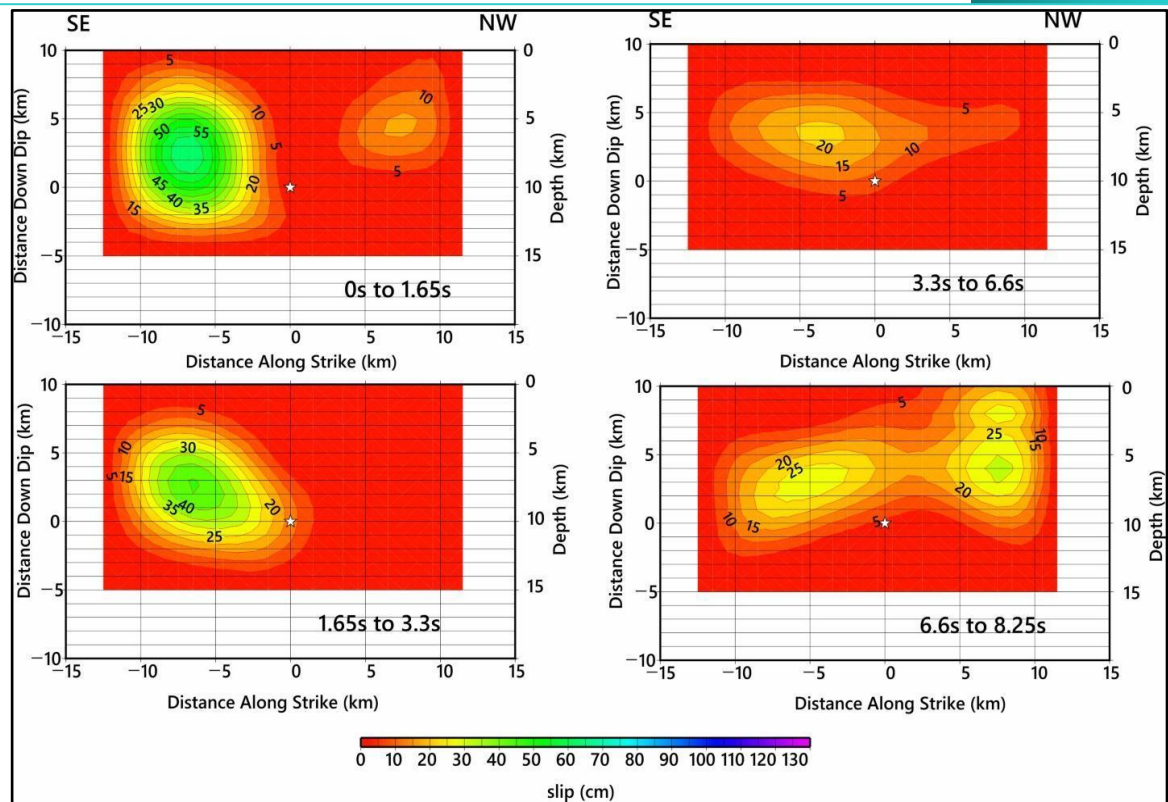


**Fig. 11:** Snapshots of the incremental evolution of rupture history, showing that mainly it propagated towards ESE, attaining a bilateral propagation at later stages. Contours depict slip amplitudes. Note the absolute depth scale on the right of each panel.

The rupture propagated towards ESE (Fig. 10) and persisted in that ESE direction until the later stages of the rupture process when it propagated mainly bilaterally. In all cases the updip propagation is evident. It is worth noting that the weak slip patch at the WNW corner, that is, at the westernmost edge of the fault, is clearly evident, even from the initial stage of the rupture. This area has subsequently ruptured during the 4 March second aftershock. Although the mechanism of its occurrence is not fully understood, the existence of many aftershocks surrounding the areas of large slip indicates the importance of the stress redistribution by the main shock.

*Main shock of 4 March 2021:* The reported focal mechanism solutions for the strongest aftershock, both by NOA and AUTH, even though determined by different methods, are remarkably compatible. Other national agencies, whose solutions are based on teleseismic modelling (GCMT for example), were not able to calculate a moment tensor, because the waveforms were obscured from another global large event that occurred at the same time. We adopted the AUTH solution and in this case, the fault plane has strike, dip, and rake angles, equal to  $287^{\circ}/30^{\circ}/-92^{\circ}$ , dipping to NE again, as the main shock. The rupture speed was constrained to be 1.7 km/s.

Figures 12 and 13 summarize the slip models for the aftershock. Slip is confined in a well-determined single asymmetric patch (Fig. 12) updip from the hypocenter, indicating a rather bilateral rupture propagation for this event. For this model parameterization the resolved seismic moment is  $1.00E18$  N m, resulting in  $M_w=5.97$  and the average slip value is 23 cm.

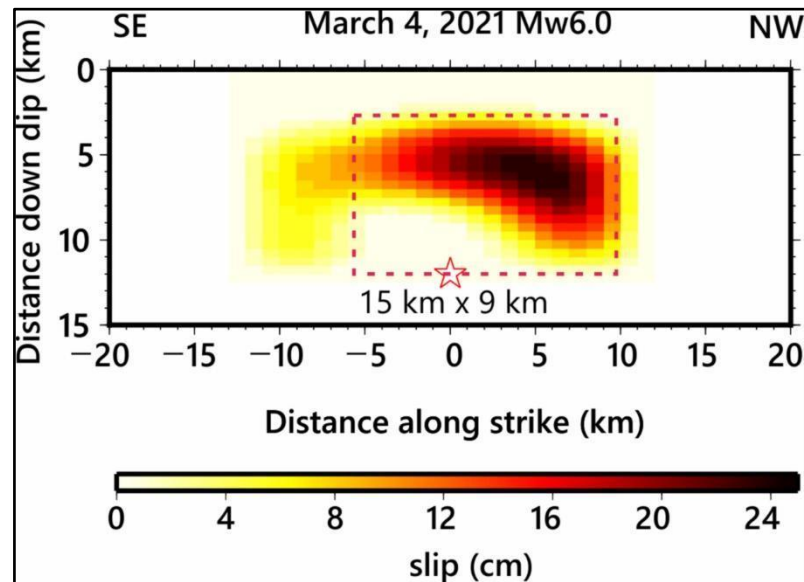


**Fig. 12:** Spatial distribution of slip for the March 4 main shock, along  $287^\circ$  fault strike direction. Slip is confined in a major slip patch (dashed rectangle) directly updip from the hypocenter (asterisk) and to its NW.

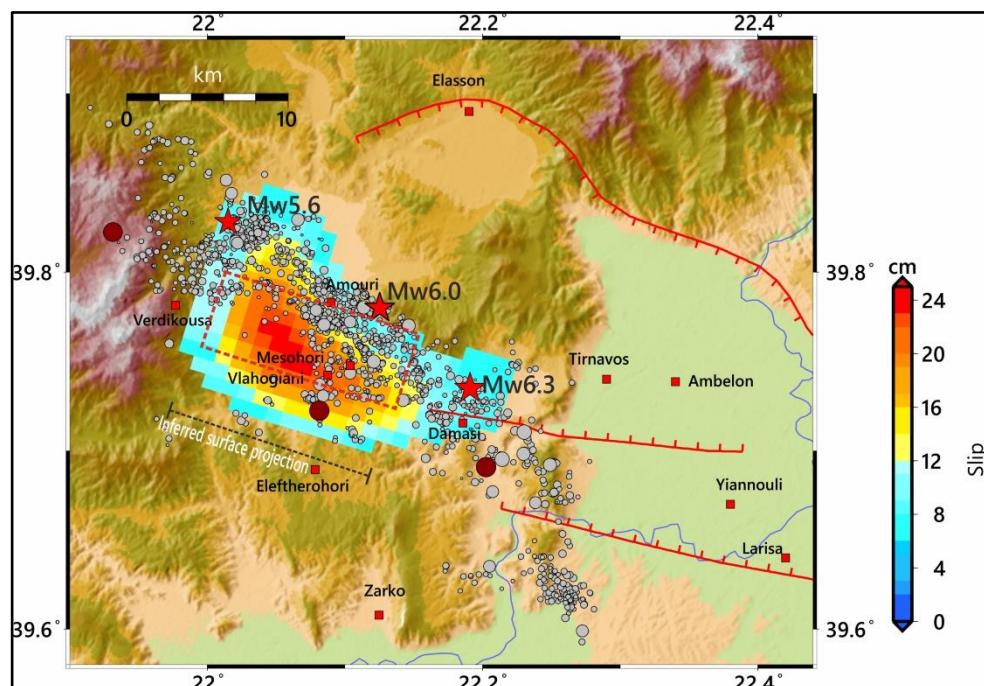


**Fig. 13:** Surface projection of the aftershock's slip model (Fig. 12) alongside relocated aftershocks (circles). A 30% trimming to the peak slip is imposed to the model for clarity. The dashed rectangle and line denote the fault that rupture and its inferred surface projection, respectively.

For the resolved moment and confining the ruptured area ( $15 \text{ km} \times 9 \text{ km}$ ) into a circular area, the Brune-type stress drop for the second main shock is 16 bars (1.6 MPa).

#### 4.4 ShakeMap of the 3 March 2021 Main shock

To examine the spatial distribution of the intensity of ground motion we used the preferred slip distribution model for the first main shock, in order to perform forward modeling and calculate synthetic velocity records. We used a grid covering the broader region (Fig. 14) and in each node we calculated two horizontal velocity records. Using the modules of SAC we depict the maximum values of each component, and we contour their arithmetic average (Fig. 14a). The synthetic values do not take into account any site-effect, as a detailed profile for the epicentral region is not available, yet.

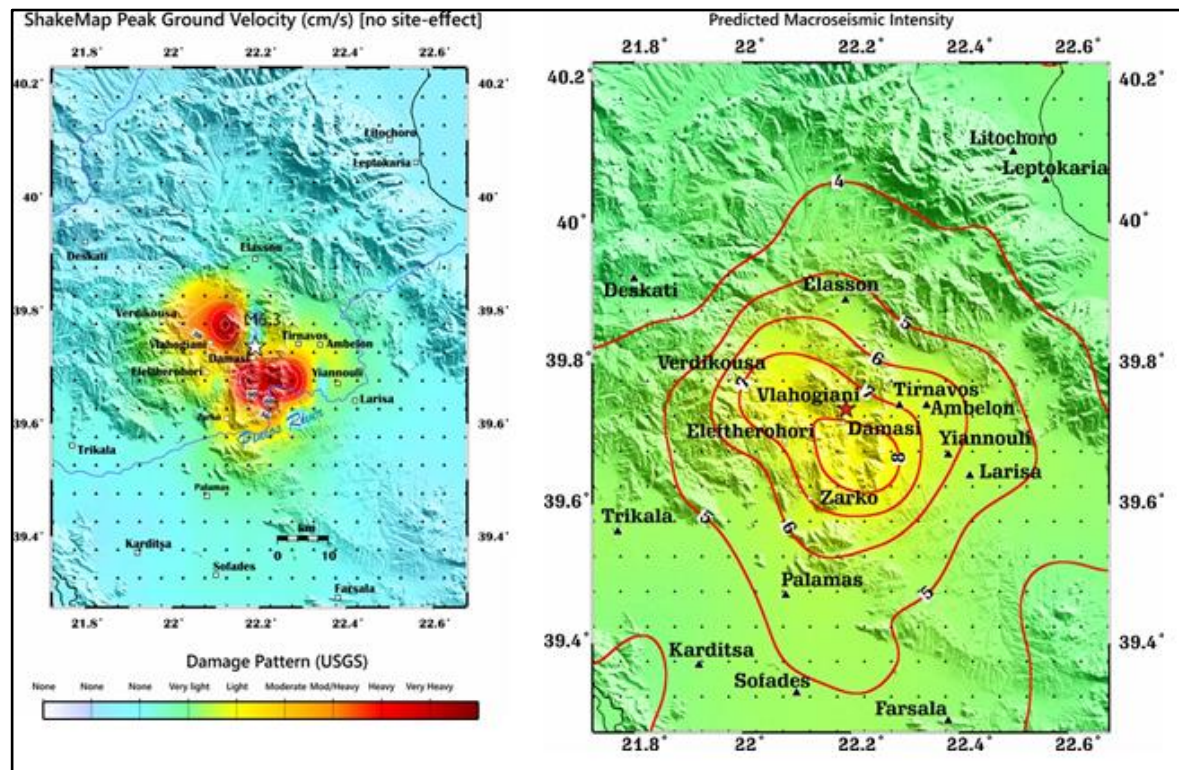


**Fig. 14:** (a) ShakeMap calculated using forward modeling and the slip model for the first main shock. (b) Predicted distribution of macroseismic intensities using suitable scaling relations for Greece (Caprio et al., 2015).

We used global scaling relations, which were obtained using extensive data from the Mediterranean (Caprio et al., 2015) to calculate predicted macroseismic intensities (Fig. 14b). We checked these predictions with reported intensities based on citizens information or calculated from observed records using scaling relations, as they are reported at the NOA website. In all cases, we found very good agreement. For example,

at the close station GINA (Giannouli), the reported intensity from NOA is VI, in accordance with our predictions. Overall, intensity 6, encloses the region which was most affected by the earthquake.

The results of Figures 14 and 15 suggest that the reliable estimation of the expected strong seismic motion level in the epicentral area requires the correct assessment of the effect of both the position of the fault and the slip model (Figure 11), but also the effect of local geology. Considering that the simulations presented in Figure 11 concern synthetic recordings of velocity up to the frequency of 2Hz, an attempt was made to calculate the strong seismic motion of the first main shock (2021-03-03,  $M_w=6.3$ ) using the stochastic finite-fault simulation approach (EXSIM algorithm, Motazedian and Atkinson, 2005; Boore, 2009). For this purpose, the geometric and kinematic characteristics of the fault of the main earthquake were employed, as they are presented in Table 3.

Initially the strong ground motion was calculated for all locations for which acceleration records were available, as well as for a dense grid (~1200 points) which covers the broader focal area, as shown in Figure 15a (area with limits 39.0–40.5° N and 21.2–23.0° E, with a step of 0.02° (~2 km) in the meizoseismal area, and a step of 0.1° in the broader area]. For these grid points, synthetic acceleration records were calculated for three soil categories, namely B, C and D according to UBC/NEHRP (practically equivalent to categories A, B and C according to EN1998-1), depending on the soil category of each simulation site (grid point). These categories were calculated from the values of the topographic slope of each grid point, since this slope has been shown to be empirically correlated to  $V_{s30}$  (Wald and Allen, 2007; Stewart et al., 2014). The slope was calculated using the digital terrain model (SRTM30), which is an updated version of the digital terrestrial model (GTOPO30), with a resolution of 30 arcsec (average spacing of ~900 m). Figure 15b shows the final distribution of the spatial variation of  $V_{s30}$ , as determined for the area of interest by the previous procedure. For each soil class, generalized amplification factors were used for soil categories B, C and D (according to UBC/NEHRP) according to Margaris and Boore (1998) and Klimis et al. (1999), which were appropriately introduced in the stochastic simulation of each simulated seismic record.

To study the effect of the slip model of Figure 10 on the results, we initially employed only the geometry of the main rupture, i.e., a normal fault with a dip of ~36°, and a strike of 315°. For this geometry, multiple rupture scenarios were considered and the average values of various parameters of the strong ground motion were calculated.

These multiple scenarios corresponded to different locations of the rupture starting point and different random models for the slip distribution along the seismic fault. Therefore, for these initial simulations, any information about the slip distribution on the fault was ignored. In this approach and for all simulation grid points, several calculations of time histories of ground acceleration have been performed, allowing the calculation of the average values of various strong ground motion parameters (e.g. PGA, PGV, etc.) for each point of the grid shown in Figure 15a.

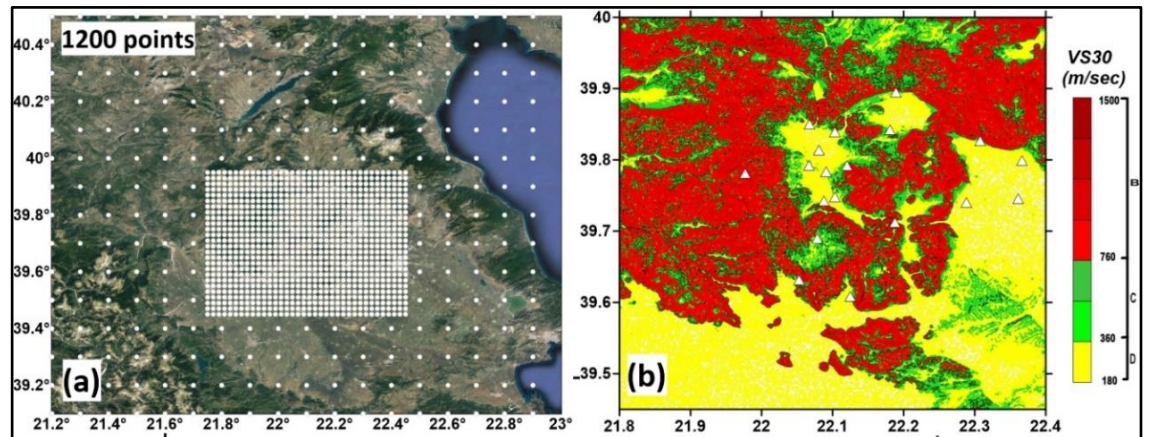


**Fig. 15:** a) Grid employed for the simulation of strong ground motion for the mainshock of the Tyrnavos sequence ( $M_w$ 6.3, 2021/03/03). b) Spatial variation of the estimated  $V_{s30}$  values in the broader Tyrnavos sequence area, as determined from the topographic slope proxy approach of Wald and Allen (2007).

Figure 16 shows the comparison between the values of the peak ground velocity (PGV) and peak ground acceleration (PGA) from accelerograph recordings with those obtained from the use of the EXSIM algorithm for the main earthquake for distances up to 100km. The comparison suggests that the stochastic simulation adequately captures the spatial distribution and the characteristics of the strong ground motion for the Tyrnavos mainshock, although in this simulation we have employed information only for the geometry of the seismic fault and a very generic approximation for the contribution of local geology site effects. It should be noted that some differences are observed between observed and predicted values, especially for peak ground acceleration (PGA), with the real (observed) values being lower (up to a factor of  $\sim 2$ ) than the synthetic ones for the random slip model. These differences, especially in the PGA values, can be attributed to several factors. However, it should be noted that most recording sites are located in basins, with a significant thickness of sedimentary deposits (e.g., Larisa, Karditsa, Volos, etc.). This increased thickness is expected to significantly affect (increase) the high-frequency attenuation factor,  $\kappa_0$ , resulting in a significant attenuation of the high-frequency energy. As a result, the predicted PGA values are systematically overestimated, since we have relied on the average (and lower) UBC/NERHP soil class

$\kappa_0$  values, as these were determined by Margaris and Boore (1998) and Klimis et al. (1999).

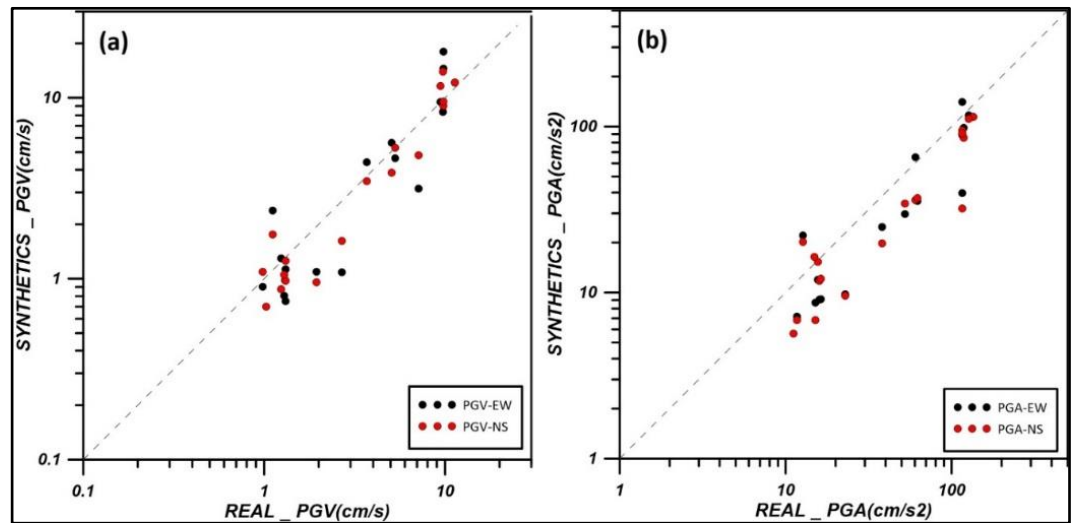


**Fig. 16:** Graphs showing the comparison of the PGV (a) and PGA (b) values, as these were determined from acceleration records ( $PGV_{Obs}$  και  $PGA_{Obs}$ ) and EXSIM results ( $PGV_{Syn}$  and  $PGA_{Syn}$ ) from the finite-fault simulation of the 3 March 2021 main shock ( $M_w 6.3$ ) using a random slip rupture scenario.

Given the adequate correlation of observed and simulated peak ground motion values (especially for peak ground velocity, PGV) at the accelerograph sites, despite of the use of a random slip rupture model, we estimated the spatial distribution of the expected PGA and PGV values in the meizoseismal area (Figures 17 and 18). In the results, we observe particularly large values of the peak ground acceleration (up to 0.7g) along the seismogenic fault, especially close to its surface projection, while large values are also observed in the area where the heaviest damage from the main earthquake was observed (e.g., Damasi village). PGA values along the area of the Titarisios river valley also reach values of the order of 0.35-0.45g (e.g., in the villages of Mesochori, Vlachogianni and Amouri) which, in combination with the influence of local soil conditions (Figure 15b), can partially explain the heavy damage observed in these settlements. Of particular interest is the area of increased PGA values near the southeastern end of the fault extension (northeast of the village of Zarko), as in the same area the highest surface subsidence values ( $\sim 35$ cm) were observed from the InSAR data. In the city of Larissa, the stochastic simulation yields PGA values of  $\sim 100$ – $150$   $cm/sec^2$ , in good agreement with the values observed in the installed accelerometers (LAR1, LAR4, S4, S5).

Regarding the values of the peak ground velocities (PGV) in the same area, we observe that in the meizoseismal area they range between 35–45  $cm/sec$ . At the borders of the surface fault projection (villages Pretorio, Domenico, Verdikousa, etc.) these values

drop to 20–30 cm/sec, while at larger distances (>20 km) from the epicentral area the PGV values reach up to ~15 cm/sec (e.g., in the city of Larissa), in good agreement with the observed values.

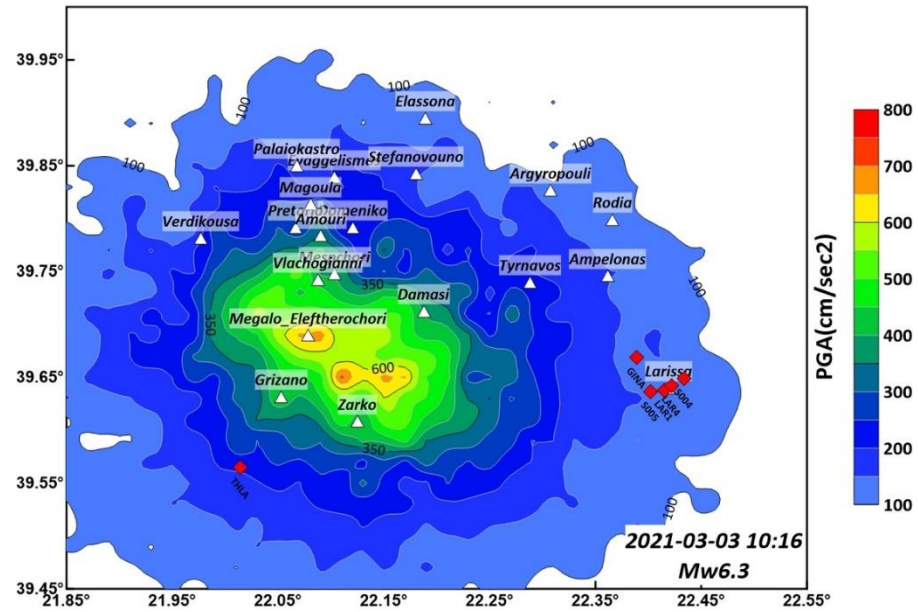


**Fig. 17:** Spatial distribution of the simulated peak ground acceleration (PGA) values in the broader Tyrnavos main shock area ( $M_w$ 6.3) for the random slip rupture model. Accelerographs for which records were available (LAR1, LAR4, S4, S5, GINA και THLA) are depicted with red diamonds.

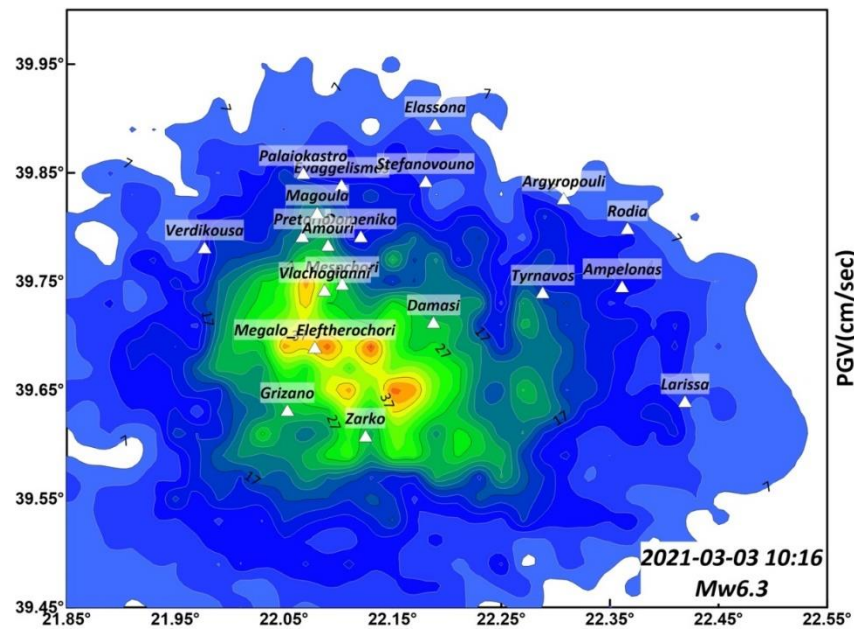


**Fig. 18:** Similar to Figure 17, for the peak ground velocity (PGV) distribution.

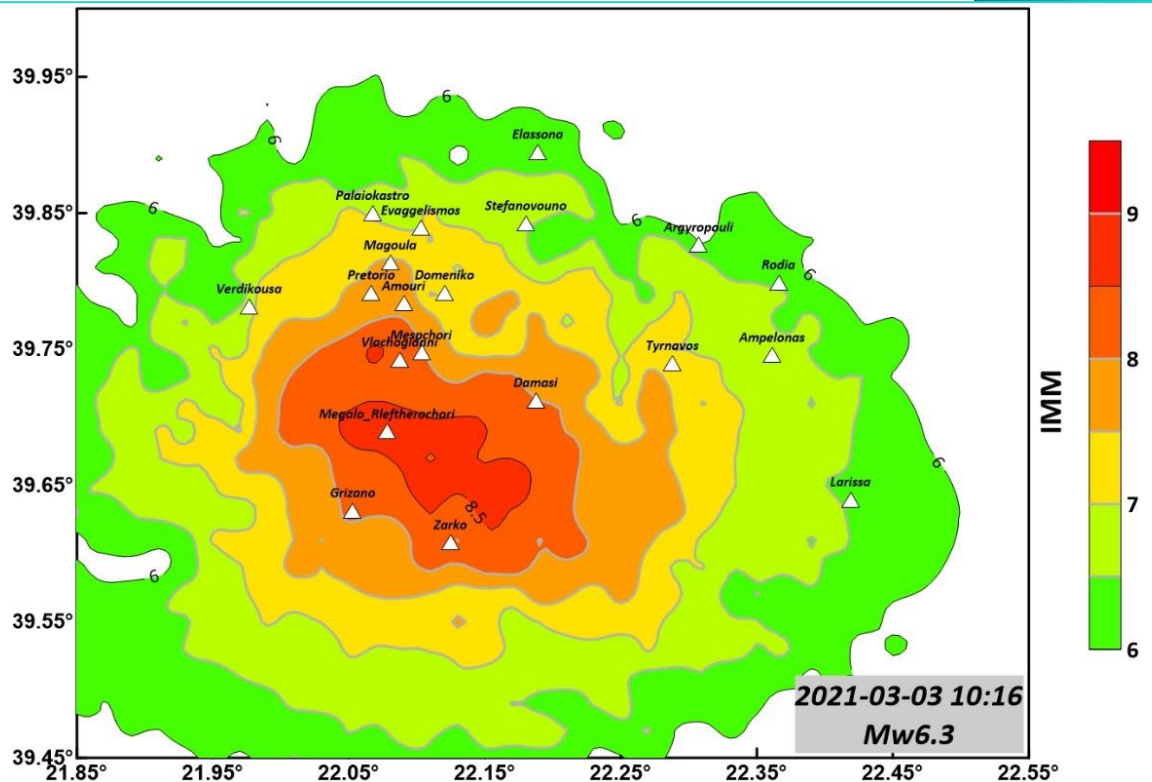


**Fig. 19:** Spatial distribution of the synthetic (simulated) macroseismic intensity values in the Modified Mercalli (IMM) scale, as determined from the PGA and PGV values from the finite-fault stochastic simulation approach for the 2021/03/03,  $M_w$ 6.3 main shock, using a random-slip rupture model.

To estimate the predicted distribution of damage for the main earthquakes of the Tyrnavos sequence ( $M_w$ 6.3), we calculated the synthetic values of macroseismic intensities in the Modified Mercalli scale (IMM) by converting and averaging the synthetic values of PGA and PGV (shown in Figures 17 and 18) into macroseismic intensity values. For the conversion we used the relationship of Wald et al. (1999), appropriately corrected for the Greek version of Modified Mercalli, according to the suggestion of Kkallas et al. (2018). The spatial distribution of the predicted (simulated) macroseismic intensities for the random slip rupture model is shown in Figure 19. It is evident that the results suffer from the same problems seen in Figures 17 and 18. More specifically, while the predicted IMM values show a general consistency with the observed damage level, the actual distribution shows particularly large values close to the surface projection of the fault, leading to very high intensity values (IMM~8.5-9) in Megalo Eleftherochori, and slightly smaller values (IMM~8-8.5) for the villages of Zarko and Grizano in the prefecture of Trikala. These values are not in agreement with the observed damages, which were significant in Zarko, but relatively limited for Grizano and especially Megalo Eleftherochori, for which the highest peak ground acceleration and velocity values are predicted (Figures 17 and 18) for the random slip rupture model.

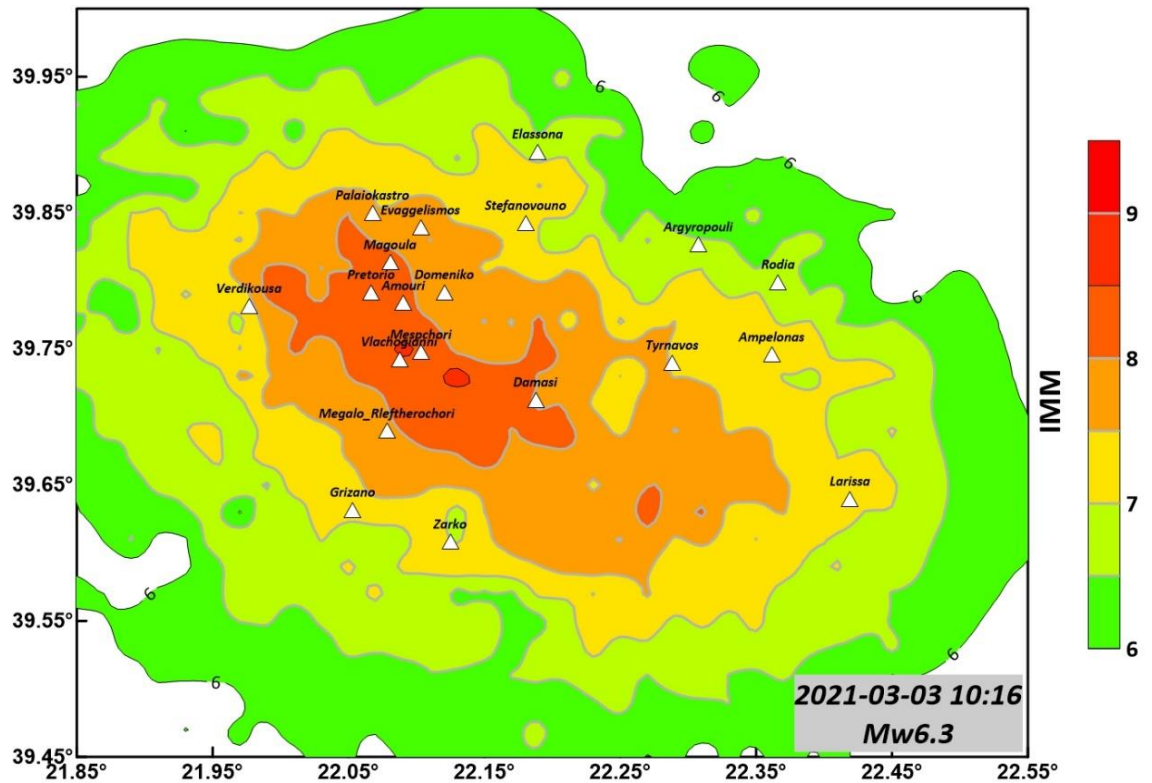


**Fig. 20:** Same as Figure 19 for the slip rupture model determined from broadband waveform inversion (see Figure 10).

For this reason, the calculations of the peak ground acceleration (PGA) and velocity (PGV) were repeated using the slip distribution model calculated from the inversion broad-band waveform data (Fig. 10), and the results were employed to calculate an updated IMM distribution. The results are presented for this new assessment of macroseismic intensity in Figure 19, leading to a much more realistic spatial distribution of the expected damage. In particular, we observe that the new slip rupture model has led to the concentration of heavy damage ( $IMM > 8$ ) values along the settlements of the Titarisios river valley, especially the villages of Damasi, Vlachogianni, Mesochori, Amouri, Pretorio and Magoula. On the contrary, a lower level of macroseismic intensity is observed for the cities of Tyrnavos and Larissa ( $IMM \sim 7.5$  and  $7$ , respectively), in very good agreement with the damage observations in these areas.

The results presented in Figures 19 and 20, and the significant differences observed depending on the rupture (slip) model adopted, suggest that the combination of the site effects from local geology along the Titarisios river basin, together with the specific pattern of rupture (slip model of Figure 11), have led to the high damage level in the specific area, as suggested by the predicted very high peak ground motion levels ( $PGA \sim 0.45-0.6g$  and  $PGV \sim 25-40cm/sec$ ). On the contrary, for the villages south of the

surface projection of the fault (Megalo Eleftherochori, Zarko and Grizano) the values of the peak strong ground motion (as expressed by PGA and PGV) for the determined slip model (Figure 10) are significantly smaller ( $PGA < 0.35g$  and  $PGV < 25$  cm/s), in comparison to the results from the random slip model, in very good agreement with the observed damage pattern in this region. In summary, the previously presented simulations confirm the suggestion that the observed distribution of damage (Figure 20) of the first main shock ( $M_w 6.3$ ) is due to the combination of three different factors that acted simultaneously:

- A) The geometry of the fault, i.e., a low angle normal fault, extending significantly over a relatively large area, hence affecting a large number of settlements
- B) The specific distribution of slip in the fault, as this is presented in the rupture model of Figure 10 and,
- C) The contribution of the local site (geology) effects, in particular the soft soil sediments with low  $V_{s30}$  values along the Titarisios river valley (Figure 15b).

While the results of Figure 20 should be considered as quite realistic, since no strong motion instrument was in operation in the meizoseismal area, it is evident that the use of more reliable and local transfer functions for the settlements mostly affected can lead to improved simulations for the observed damage distribution. This is especially critical for small spatial scales, since significant differences of observed strong ground motion levels at different sections of the various settlements have been documented, on the basis of observed damage variability (e.g., lower and upper part of the village of Damasi, etc.).

## 5. EARTH OBSERVATION DATA & SAR INTERFEROMETRIC PROCESSING

The analysis was based on open and free Sentinel-1 C-band Synthetic Aperture Radar (SAR) data. The Sentinel-1 mission, based upon a pre-defined and conflict-free acquisition plan, is able to systematically provide a large volume of SAR imagery, typically less than 4 hours from sensing, via the Copernicus Open Access Hub (<https://scihub.copernicus.eu>) since October 2014. The above fact ensures global coverage in a relatively short time, a major advantage when rapid response is intended as demonstrated after various strong earthquakes (Cornou et al., 2020; Foumelis et al., 2021). For the case of 2021, March 3 main shock the broader epicentral area, as defined by initial seismological measurements, was mapped in less than 12 hours from its

occurrence, facilitating the rapid mapping of the affected zones, as well as the investigation, separately, of the stronger earthquakes of the seismic sequence.

Interferometric processing was undertaken on a Virtual Machine (VM) provided by the ESA RSS–Cloud Toolbox service (Marchetti et al., 2012), having direct access to the Copernicus archives via the CREODIAS infrastructure (<https://creodias.eu>). For the processing, the GAMMA software packages were used (Wegmüller et al., 2016). To compensate for the topographic component, heights from the AW3D30 DSM (Takaku et al., 2018) were utilized. The applied InSAR processing scheme has been well–demonstrated in several environments for measuring ground displacements (Papanikolaou et al., 2010; Lemoine et al., 2020). Utilizing interferometric pairs of short temporal separation (between 6 and 18 days), high coherence levels are ensured, minimizing measurements uncertainties. Regions exhibiting interferometric coherence levels below 0.3 were excluded from further analysis, as being non–valid DInSAR measurements. Although often related to temporal decorrelation, in that case, and especially for the 6-days pairs, low coherence regions were collocated to secondary earthquake phenomena, mostly liquefactions, surface ruptures and regions exhibiting highly distributed deformation (i.e. nearby observed ground motion maxima).

The major advantage of the systematic availability of EO data guaranteed the successful mapping of the earthquake–induced ground displacements. The acquisition dates of the satellite for track A120 versus the occurrence of major events was the most favorable for the investigation of the displacement field as caused by each of these earthquakes (Fig. 21).

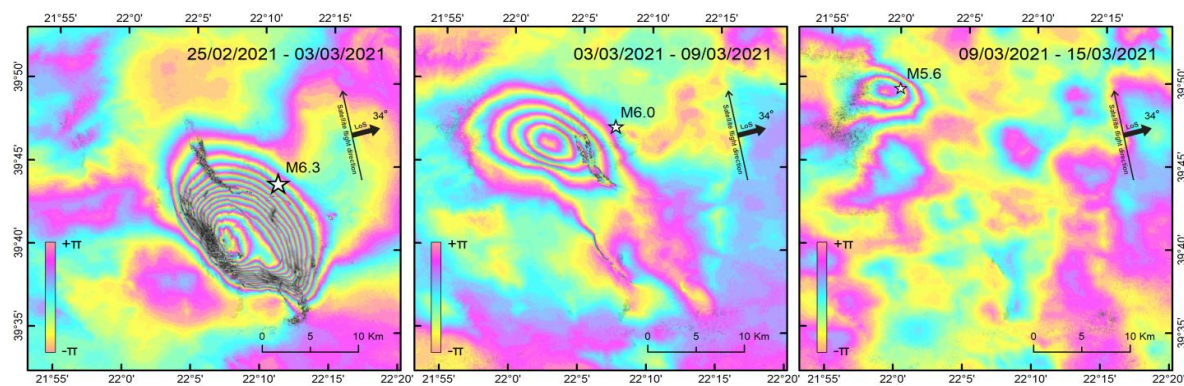


**Fig. 21:** Sentinel–1 6–days differential wrapped interferograms (ascending track 102) of time spans comprising the stronger earthquakes of the Tynavos 2021 sequence,  $M_w$ 6.3 (left),  $M_w$ 6.0 (center) and  $M_w$ 5.6 (right). Regions of low interferometric coherence ( $\leq 0.3$ ), non–valid DInSAR measurements, appear as black.

As observed by DInSAR, the maximum ground displacement reached -38 cm for the M6.3 mainshock (negative value indicate ground subsidence or motion away from the satellite), whereas lower values of -12 cm for the M6.0 and -9cm for the M5.6 events were calculated, representing respectively 32% and 24% of the total motion caused by the first mainshock.

The first main shock displacement field, as shown by the interferometric fringes (Fig. 21), represents an elliptical shape elongated at NW–SE direction, whereas for the second M6.0 main shock a counterclockwise rotation is observed with the ellipse being less elongated (reduced length of semi-major axis). For the M5.6 event, the interferometric fringes become more circular with elongation along a WNW–ESE direction. Common to all events is the fact that rupture zones do not seem to propagate to the surface, since no discontinuity of the interferometric fringes was recognized. This consorts with the upper limit of the seismogenic layer as defined by the relocated aftershocks.

## 6. GNSS DATA AND SITE DISPLACEMENT ESTIMATION

Dual frequency data were processed from five (5) permanent GNSS stations located close to the epicenter of the March 3 main shock that receive signals from the Global Satellite Navigation Satellite Systems (GNSS). The data time span cover about two weeks from March 1 to March 14, 2021. The stations belong to the HermesNet of Auth (Fotiou et.al., 2009, Fotiou and Pikridas 2012), HeXGon/SmartNet-Greece and NOANet (Chousianitis et al., 2021). The location distribution of GNSS stations is relatively optimal as they extend mainly around the epicenter area of each earthquake.

Data analysis was based on 30–sec daily GPS+Glonass observations and elevation cut–off angle  $10^\circ$  and therefore provided important data for depict the field of motion during the earthquakes and were included in our analysis. Four out of the five stations record GPS and Glonass data which is an advance for the impact of Satellite geometry in the process. The process was held on the current reference frame ITRF2014 using the web–based PPP platform of National Resources of Canada–Canadian Geodetic Survey (CGS). The well–known CSRS–PPP is an online application for data post–processing allowing users to compute higher accuracy positions from their GNSS raw data. Daily position coordinates are estimated on the International Terrestrial Reference Frame 2014 (ITRF2014) where positional accuracy is characterized by sub–centimeter, which fulfills the appropriate level for our study. The daily calculated displacements expressed in the topocentric system (East, North, Up) are presented in Table 4.

**Table 4.** Coseismic and cumulative displacements during Tyrnavos aftershock sequence between 1 and 14 March 2021.

Earthquakes	E N Up displacement (in cm)	Permanent GNSS station				
		ELAS $\varphi=39^{\circ}53'32''.7$ $\lambda=22^{\circ}12'22''.1$	KLOK $\varphi=39^{\circ}33'53''.3$ $\lambda=22^{\circ}00'51''.4$	LARM $\varphi=39^{\circ}36'50''.7$ $\lambda=22^{\circ}23'16''.4$	KRDI $\varphi=39^{\circ}21'59''.34$ $\lambda=21^{\circ}55'21''.48$	MURG $\varphi=39^{\circ}44'19''.3$ $\lambda=21^{\circ}33'15''.1$
<b>March 03, 2021 10:16 AM</b>	dE	1.0	-	0.3	-1.1	-0.2
	dN	3.3	-	0.0	0.2	-0.2
	dUp	-1.4	-	-0.2	0.3	1.2
<b>March 03, 2021 06:24:00 PM</b>	dE	0.5	-	0.3	-0.5	-0.6
	dN	0.7	-	0.1	-0.6	0.4
	dUp	-0.3	-	-1.1	-1.7	-1.1
<b>March 12, 2021 12:57:00 PM</b>	dE	0.5	-0.1	-0.5	-0.3	0.5
	dN	0.7	0.1	0.5	-0.5	0.5
	dUp	0.1	-0.2	-0.3	0.5	1.5
<b>March 04, 2021 07:23:00 PM</b>	dE	-0.1	-0.3	0.0	1.1	-1.0
	dN	0.1	-0.1	0.1	-2.0	1.0
	dUp	0.4	0.1	0.6	1.0	-0.6
<b>March 04, 2021 06:38:00 PM</b>	dE	0.4	0.0	-0.2	-0.9	-0.4
	dN	1.5	-0.7	0.5	-0.5	0.5
	dUp	0.3	-0.6	-1.6	-0.3	1.2
<b>Cumulative Disp. between 1 – 14 March</b>	dE	<b>2.2</b>	<b>-3.4</b>	<b>0.1</b>	<b>-0.3</b>	<b>-0.4</b>
	dN	<b>4.3</b>	<b>-4.0</b>	<b>0.5</b>	<b>-1.1</b>	<b>-0.2</b>
	dUp	<b>1.4</b>	<b>0.3</b>	<b>1.4</b>	<b>2.4</b>	<b>2.6</b>

After examining the effect of each earthquake in the coordinates stability, it was found out that the strongest co-seismic displacement was observed in the Ellassona GPS/GNSS station (ELAS) which is located ~18 km from the first main shock epicenter (March 03, 2021, 10:16 AM), with a value of 3.3 cm on the north-south topocentric component. It must be noted that due to data availability, it was not possible to estimate co-seismic displacements for Klokotos (KLOK) site regarding the first two earthquakes. The most notable results are observed in ELAS and KLOK stations, as we may see at the cumulative displacements, which are estimated between 1 to 14 March (see Table 4). The estimated results were also confirmed from the related analysis of

Interferometric Synthetic Aperture Radar – InSAR data where similar displacements were calculated. At this point we must refer that GNSS data indicates high accuracy pinpoint displacements estimation while the InSAR technique depicts areal deformation pattern.

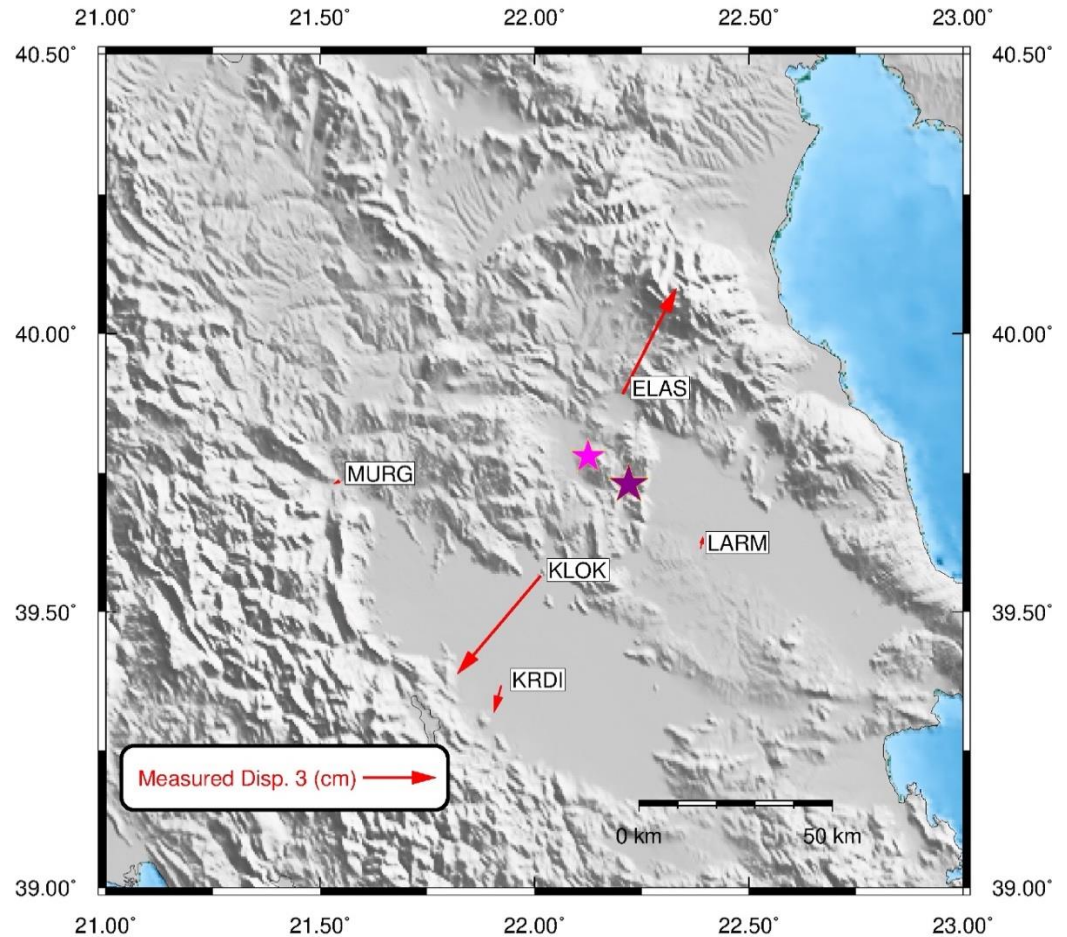


**Fig. 22:** Cumulative coseismic displacements between 1 and 14 March 2021 from the GNSS network in the study area.

## 7. STRESS INTERACTION OF THE SEQUENCE

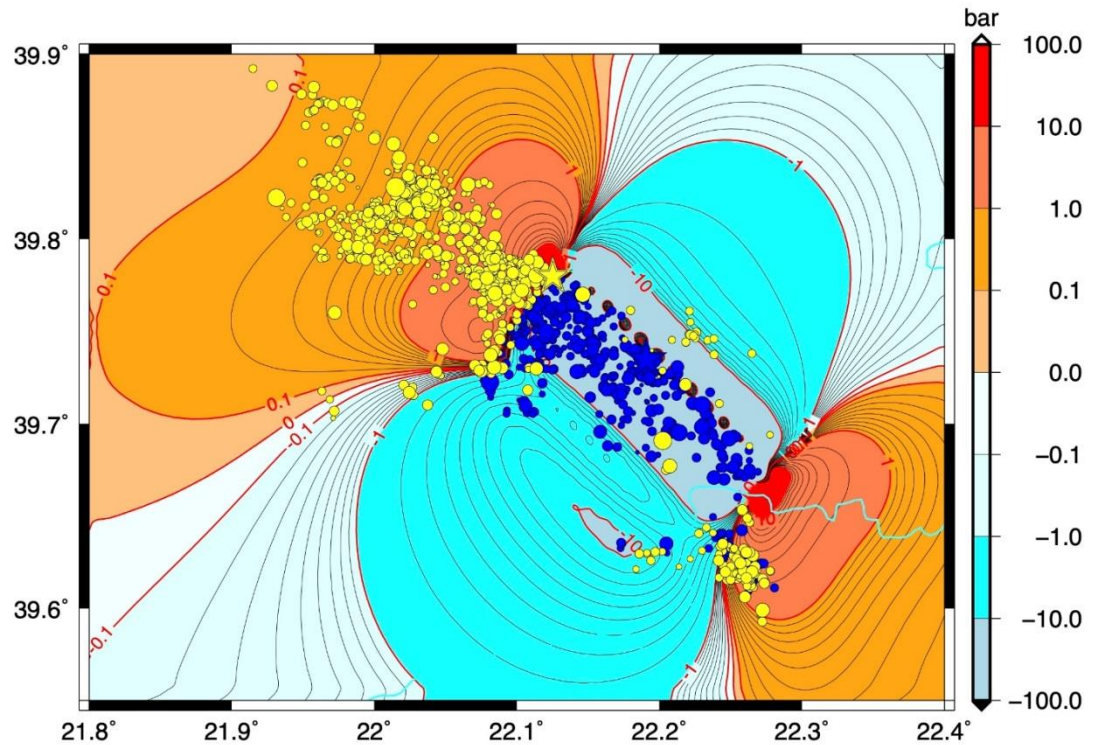
There is convincing evidence, even accompanied with limited skepticism, that static Coulomb stress transfer can promote and inhibit subsequent seismicity. To unveil the cascading occurrence of the aftershock seismicity we calculate the Coulomb stress change,  $\Delta CFF$ , caused by the first main shock. With simplifying assumptions to account for pore pressure effects,  $\Delta CFF$  is given by (King et al., 1994):

$$\Delta CFF = \Delta\tau + \mu' \Delta\sigma_n \quad (1)$$

where  $\Delta\tau$  is the shear stress change on the target fault (positive in the direction of fault slip),  $\Delta\sigma_n$  is the fault normal stress change (positive when unclamped), and  $\mu'$  is the effective coefficient of friction (which implicitly includes the unknown pore pressure change on the fault).

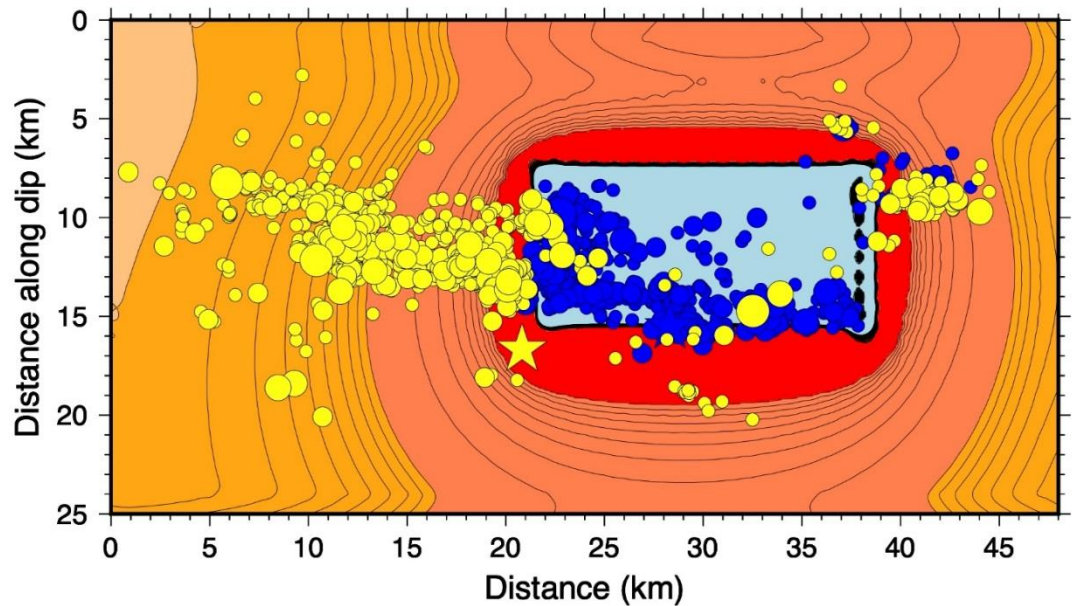
The Coulomb hypothesis holds that earthquakes are promoted when  $\Delta\text{CFF}$  is positive, and they are inhibited when  $\Delta\text{CFF}$  is negative. There are numerous publications in the past 20 years, where this hypothesis has been tested and has been largely upheld for aftershock sequences (e.g., Karakostas et al., 2003; Papadimitriou et al., 2017) and sequential strong ( $M \geq 6.2$  or  $M \geq 7.0$ ) earthquake occurrence (e.g., Papadimitriou, 2002; Paradisopoulou et al., 2010). For the study area in particular, it has been shown that the episodic occurrence of  $M \geq 6.2$  earthquakes, in remarkably active periods alternated with long lasting relative quiescence periods, is well supported by stress transfer among adjacent or closely located fault segments (Papadimitriou and Karakostas, 2003). The closeness in space and time of the two mainshocks evidence possible triggering through stress transfer. This observation along with the off-fault aftershocks that imply the activation of multiple minor fault segments, invites the comparison of spatial aftershock distribution with Coulomb stress changes. We seek to understand earthquake interaction on the 30 hours between the two main shocks and then the aftershocks, in a three dimensional stress changes pattern.

Figure 23 shows on a map view the Coulomb stress changes due to the coseismic slip of the March 3 main shock, calculated at a depth of 9 km (a little bit shallower than the nominal depth of the  $M_w 6.3$  earthquake, which equals to 9.5 km). Planar rectangular surface was assumed for the causative fault, and the source parameters for the first mainshock as defined in the previous sections ( $L=17$  km,  $w=8$  km, mean coseismic slip=0.70 m). The aftershock epicenters are depicted by circles with size proportional to the event magnitude, alike the representation in the map depicting the aftershock epicentral distribution. Yellow and blue colors were selected to signify positive and negative  $\Delta\text{CFF}$  values that are calculated at the focus of each aftershock. The epicenters of the March 4 main shock and all following aftershocks are located inside stress enhanced areas. Perhaps the 30 hr delay is in some sense a product of a cascade of aftershocks, and not strictly the stress transfer from the first mainshock to the second. The fact that some epicenters colored as receiving positive stress changes (colored in yellow) are located in stress inhibited areas and vice versa, happens because these epicenters are projected at the depth of 9 km. Earthquakes with focal depths quite different than 9 km, might be assigned different  $\Delta\text{CFF}$  value than the one calculated at this position onto the horizontal plane at the depth of 9 km.



**Fig. 23:** Coulomb stress changes due to the coseismic slip of the March 3 ( $M_w$ 6.3) main shock, resolved according to its faulting type (strike/dip/rake=314°/36°/-88°) onto a horizontal plane at a depth of 9 km. Circles of different size depict the relocated aftershocks in the first 30 hrs. between the two main shocks. The star shows the epicenter of the March 4 ( $M_w$ 6.0) main shock, which is located at a site where the positive  $\Delta$ CFF attain their largest value.

Figure 24 shows the Coulomb stress changes onto a plane parallel to the first rupture plane, according to the same color scale as in Figure 23. The cross-section direction is NW-SE, and the first main shock area coincides with the area where the negative  $\Delta$ CFF changes attain values as small as -10 bar. The color of the projected hypocenters has been selected with the same criteria as before (Fig. 23). It is impressive that the vast majority of aftershocks occurred in stress enhanced areas. The negative  $\Delta$ CFF values that are calculated at some aftershocks foci might be attributed to the simplified slip model with a uniform slip onto a planar surface, diverse of fault orientation even for the small aftershocks, relocation errors, or combination of the above. Figure 24 shows that not only was the site of the  $M_w$ 6.0 hypocenter promoted by stress transfer, but aftershock seismicity in areas of negative  $\Delta$ CFF was inhibited. The southern distinctive cluster that was noticed and mentioned in the spatial and temporal aftershock distribution, is clearly shown here that is entirely located in stress enhanced areas and is shallower than the other aftershock concentrations. This offers one more clue that it concerns an independent minor fault segment.



**Fig. 24:** Stress imparted by the first main shock ( $M_w$ 6.3, 3 March 2021, white star), resolved onto a plane parallel its rupture plane and for its faulting parameters (strike/dip/rake= $314^\circ/36^\circ/-88^\circ$ ). All earthquakes are projected onto this plane (after considering their focal depths and dip angle of the projection plane). Aftershocks in the first 30 hours (before the second main shock of  $M_w$ 6.0, 4 March 2021) are plotted in white, whereas after that time in yellow. The second main shock (yellow star) is nucleated at an area where the positive Coulomb stress exceeds 10.0 bars.

## 8. DISCUSSION AND CONCLUSIONS

Our results suggest that the 2021 doublet ruptured previously unmapped fault segments with the majority of slip in the two main shocks to the west of the town of Tyrnavos. The activity mainly propagated northward from the first main shock epicenter, rupturing a crustal volume roughly between 4 and 15 km and shallower off-fault seismicity. The predominantly normal mechanism of the two main shocks, the stronger ( $M \geq 5.0$ ) aftershocks and the overall sequence, all suggest a style of faulting controlled by extensional mechanism. Although there is little evidence for historic seismicity along these fault segments that turned up capable of hosting strong ( $M \geq 6.0$ ) earthquakes, they exhibit similar faulting style and along with the neighboring mapped faults they appear rupturing members of a fault system that bounds the western margin of the eastern Thessalia basin, composing an extensional fault population alike in other areas in back arc Aegean region.

This seismic excitation signifies that  $M_w$ 6.0 earthquakes can occur on relatively minor fault systems throughout the Greek territory and that often these minor fault systems

have not been well characterized. Additionally, one more conclusion is that earthquakes of this magnitude can cause substantial ground motions resulting in significant damage to constructions that were not built according to the current building code standards.

The relocation of the two main shocks and more than ~1450 aftershocks, extending from 4 to 15 km depth, outline the spatiotemporal evolution of the seismic sequence and the geometry of the ruptured fault network. Improved understanding of the aftershock sequence has become possible with the inclusion of data from the temporary monitoring network. The expansion of the aftershock spatial distribution far beyond the edges of the two main ruptures, supports the idea of a volumetric strain release process. The focal mechanisms and the aftershock spatial distribution agreed and documented the NW–SE striking and northeast dipping fault planes, of moderate dip. Additional distinctive seismicity clusters and seismicity clouds may give clues for the origin of other seismicity streaks implying minor conjugate faults activation, most probably triggered by stress transfer of the major events of the sequence.

The kinematic finite–fault rupture models calculated for the mainshock and the strongest aftershock, showed that the major slip is well–confined in slip patches (asperities). In both cases, the rupture initiated from the bottom of the fault and propagated updip. For the mainshock, if any directivity is present, then it should mainly be towards SE, towards the town of Zarko. For the aftershock, the models support rather bilateral propagation. An interesting feature observed in both models is the fact that the major slip is confined in the upper crust and in the middle of the seismogenic layer approximately between 3 and 7 km, whereas the slip in the uppermost few kilometers is systematically less compared to greater depths. This was also observed in several recent earthquakes in the Aegean area (Kiratzi, 2018; Karakostas et al., 2021; among others). Keeping in mind that this may be an artifact of the smoothing and regularization imposed to stabilize the inversion, nevertheless this observation is also supported by the cross-sections of the relocated aftershocks, pointing to different elastic properties of the uppermost part of the crust. Another observation, regarding the kinematic models of the mainshock and the strongest aftershock, is the relatively slow velocities ( $< 2.5$  km/s) required to fit the data (which is less than 70% of the  $V_s$  velocity at the source depths). Such slow rupture speeds have been observed elsewhere (Wang et al., 2020) and they are mainly interpreted due to rupture on relatively immature fault systems (Liu et al., 2019 and references therein).

Coulomb stress changes due to the coseismic slip of the first main shock, are resolved at the focus of each aftershock. The results are projected on a map view also depicting

the  $\Delta CFF$  calculated at a depth of 9 km, along with onto a plane almost parallel to the planar surfaces approximated the fault planes of the two main shocks, for more detailing the vertical aftershock spatial distribution and comparing with the respective areas of positive and negative stress changes. It is derived that the onto fault aftershocks are limited to the lower southern part of the fault surface of the first main shock, whereas, in general the aftershocks occupy the entire seismogenic layer. This observation is attributed to the maximum slip fault patch (Fig. 10) at the southern upper part of the fault. The off-fault aftershocks are all well correlated with the larger positive values of Coulomb stress changes. For the distinctive clusters in particular, it became now more evident in these projections that they are associated with triggered minor faults located in different depths.

## 9. ACKNOWLEDGMENTS

The critical review and editorial assistance of Dr. A. Ganas along with one anonymous reviewer are greatly appreciated. The software Generic Mapping Tools was used to plot some of the maps (Wessel et al. 2013). The authors affiliated with the Department of Geophysics, of the Aristotle University of Thessaloniki, acknowledge support of this work by the project “HELPOS–Hellenic System for Lithosphere Monitoring” (MIS 5002697) which is implemented under the Action “[Reinforcement of the Research and Innovation Infrastructure](#)”, funded by the Operational Programme "Competitiveness, Entrepreneurship and Innovation" (NSRF 2014–2020) and co-financed by Greece and the European Union (European Regional Development Fund). Geophysics Department Contribution 953.

## 10. DATA AND RESOURCES

The seismic waveforms from broad-band and strong motion stations of the Greek network were downloaded from the ORFEUS EIDA nodes. The macroseismic data and the ShakeMap, and the other products were retrieved download from NOA, from the site [https://accelnet.gein.noa.gr/noa\\_sites/noa.shakemaps.gr/public/index/126579](https://accelnet.gein.noa.gr/noa_sites/noa.shakemaps.gr/public/index/126579).

## 11. REFERENCES

- Abers, G. A., Mutter, C. Z. and Fang, J., 1997. Shallow dips of normal faults during rapid extension: Earthquakes in the Woodlark – D'Entrecasteaux rift system, Papua New Guinea. *Journal Geophysical Research*, 102, 15,301–15,317.
- Aristotle University of Thessaloniki, 1981. Aristotle University of Thessaloniki seismological network. *Inter. Fed. Dig. Seis. Net.* doi:10.7914/SN/HT
- Benetatos, C., Dreger, D. and Kiratzi, A., 2007. Complex and segmented rupture associated with the 14 August 2003  $M_w$ 6.2 Lefkada, Ionian Islands, earthquake. *Bulletin of the Seismological Society of America*, 97, 35–51.
- Boore, D. M., 2009. Comparing Stochastic Point-Source and Finite-Source Ground-Motion Simulations: SMSIM and EXSIM. *Bulletin of the Seismological Society of America*, 99(6), 3202-3216, doi:10.1785/0120090056.
- Caprio, M., Tarigan, B., Worden, B., Wiemer, S., and Wald, D., 2015. Ground Motion to Intensity Conversion Equations (GMICEs): A Global Relationship and Evaluation of Regional Dependency. *Bulletin of the Seismological Society of America*, 105, doi: 10.1785/0120140286
- Caputo, R., 1990. Geological and structural study of the recent and active brittle deformation of the Neogene–Quaternary basins of Thessaly (Greece). *Scientific Annals*, 12, Aristotle University of Thessaloniki, Thessaloniki. 2 vols., 5 encl. 252 pp.
- Caputo, R., and Pavlides, S., 1993. Late Cenozoic geodynamic evolution of Thessaly and surroundings (central–northern Greece). *Tectonophysics* 223, 339–362. doi:10.1016/0040-1951(93)90144-9
- Caputo, R., Helly, B., Pavlides, S. and Papadopoulos, G., 2004. Palaeoseismological investigation of the Tyrnavos Fault (Thessaly, Central Greece). *Tectonophysics*, 394, 1–20. <https://doi.org/10.1016/j.tecto.2004.07.047>
- Caputo, R., Helly, B., Pavlides, S., Papadopoulos, G., 2006. Archaeo- and palaeoseismological investigations in Northern Thessaly (Greece): Insights for the seismic potential of the region. *Natural Hazards*, 39, 195–212, <https://doi.org/10.1007/s11069-006-0023-9>

Chousianitis, K., Papanikolaou X., Drakatos G., and Tselentis, G.–A., 2021. NOANET: A Continuously Operating GNSS Network for Solid–Earth Sciences in Greece. *Seismological Research Letters*, XX, 1–15, doi: 10.1785/0220200340.

Cornou, C., Aubert, C., Audin, L., Ampuero, J-P., Baize, S., Brenguier, F., Causse, M., Chlieh, M., Combey, A., Delouis, B., Deschamps, A., Ferry, M., Foumelis, M. et al. (83 authors), 2020. Rapid response to the  $M_w$ 4.9 earthquake of November 11, 2019 in Le Teil, Lower Rhône Valley, France. *Comptes Rendus Géosciences*, doi: 10.31219/osf.io/3afs5.

Dreger, D. and Kaverina, A., 2000. Seismic remote sensing for the earthquake source process and near-source strong shaking: a case study of the October 16, 1999 Hector Mine earthquake, *Geophysical Research Letters*, 27, 1941–1944.

Fotiou, A. and Pikridas, C., 2012. GPS and Geodetic Applications, Editions Ziti, Thessaloniki. ISBN:978-960-456-346-3.

Fotiou, A., Pikridas, C., Rossikopoulos, D., Spatalas, S., Tsioukas, V., Katsougiannopoulos, S., 2009. The Hermes GNSS NtripCaster of AUTH., *Bulletin Geodesy Geophysics*, 69, <https://doi.org/refwid:18241>

Foumelis, M., Papazachos, C., Papadimitriou, E., Karakostas, V., Ampatzidis, D., Moschopoulos, G., Kostoglou, A., Ilieva, M., Minos-Minopoulos, D., Mouratidis, A., Kkallas, C., Chatzipetros, A., 2021. On Rapid Multidisciplinary Response Aspects for Samos 2020 M7.0 Earthquake. *Acta Geophysica*, <https://doi.org/10.1007/s11600-021-00578-6>

Ganas, A., 2020. NOAFAULTS KMZ layer Version 3.0 (2020 update) (Version V3.0) [Data set]. Zenodo. <http://doi.org/10.5281/zenodo.4304613>

Ganas, A., Valkaniotis, S., Tsironi, V., Karasante, I., Elias, P., Kapetanidis, V., Kassaras, I., Papathanassiou, G., Briole, P., 2021. The March 2021 seismic sequence in Larisa – Damasi, Thessaly (central Greece), its seismotectonic characteristics and geodynamic effects. <https://doi.org/10.5281/ZENODO.4617264>.

Goldsworthy, M., Jackson, J., Haines, J., 2002. The continuity of active fault systems in Greece, *Geophysical Journal International*, 148, 596–618.

Hartzell, S. H., and Heaton, T. H., 1983. Inversion of strong ground motion and teleseismic waveform data for the fault rupture history of the 1979 Imperial Valley, California, earthquake, *Bulletin of the Seismological Society of America*, 73, 1553–1583.

Heimann, S., Kriegerowski, M., Isken, M., Cesca, S., Daout, S., Grigoli, F., Juretzek, C., Megies, T., Nooshiri, N., Steinberg, A., Sudhaus, H., Vasyura-Bathke, H., Willey, T., Dahm, T. 2017. Pyrocko – An open-source seismology toolbox and library. V. 0.3. GFZ Data Serv. <http://doi.org/10.5880/GFZ.2.1.2017.001>

Heimann, S., Isken, M., Kühn, D., Sudhaus, H., Steinberg, A., Vasyura-Bathke, H., Daout, S., Cesca, S., Dahm, T., 2018. Grond – A probabilistic earthquake source inversion framework. V. 1.0. *GFZ Data Serv.* <https://doi.org/10.5880/GFZ.2.1.2018.003>

Kaverina, A., D. Dreger, and Price, E., 2002. The combined inversion of seismic and geodetic data for the source process of the 16 October 1999  $M_w$ 7.1 Hector Mine, California, Earthquake, *Bulletin of the Seismological Society of America*, 92, 1266–1280.

Karakostas, V. G., Papadimitriou, E. E., Karakaisis, G. F., Papazachos, C. B., Scordilis, E. M., Vargemezis, G., and Aidona, E., 2003. The 2001 Skyros, northern Aegean, Greece, earthquake sequence: Off-fault aftershocks, tectonic implications, and seismicity triggering. *Geophysical Research Letters*, 30(1), 1012, doi:10.1029/2002GL015814

Karakostas, V., Tan, O., Kostoglou, A., Papadimitriou, E. and Bonatis, P., 2021. Seismotectonic implications of the 2020 Samos, Greece,  $M_w$ 7.0 mainshock based on high-relocation and source slip model. *Acta Geophysica*, <https://doi.org/10.1007/s11600-021-00580-y>

Kilias, A., Frisch, W., Avgerinas, A., Dunkl, I., Falalakis, G., Gawlick, H.-J., 2010. Alpine architecture and kinematics of deformation of the northern Pelagonian nappe pile in the Hellenides. *Austrian Journal of Earth Sciences*, 103, 4–28.

Kilias, A., Thomaidou, E., Katrivanos, E., Vamvaka, A., Fassoulas, C., Pipera, K., Falalakis, G., Avgerinas, S., Sfeikos, A., 2016. A geological cross-section through

Northern Greece from Pindos to Rhodope mountain ranges: A field guide across the external and internal Hellenides. *Journal Virtual Explorer*, 50, 1–107, <https://doi.org/10.3809/jvirtex.2016.08685>

King, G.C.P., Stein, R.S. and Lin, J., 1994. Static stress changes and the triggering of earthquakes. *Bulletin of the Seismological Society of America*, 84, 935–953.

Kiratzi, A., 2018. The 12 June 2018 Lesvos Island (Aegean Sea) earthquake: Slip model and directivity estimated with finite–fault inversion. *Tectonophysics*, 724–725, 1–10, <https://doi.org/10.1016/j.tecto.2018.01.003>

Kissling, E., Ellsworth, W.L., Eberhart–Phillips, D., Kradolfer, U., 1994. Initial reference models in local earthquake tomography. *Journal Geophysical Research*, 99, doi: 10.1029/93JB03138.

Kkallas, Ch., Papazachos C.B., Boore D., Ventouzi Ch., and Margaritis, B.N., 2018. Historical intermediate-depth earthquakes in the southern Aegean Sea Benioff zone: Modeling their anomalous macroseismic patterns with stochastic ground-motion simulations, *Bulletin Earthquake Engineering*, doi: 10.1007/2Fs10518-018-0342

Klein, F. W., 2002. User’s Guide to HYPOINVERSE–2000, a Fortran program to solve earthquake locations and magnitudes. *U. S. Geological Survey Open File Report* 02–171, Version 1.0.

Klimis, N., Margaritis, B., and Koliopoulos, P., 1999. Site Dependent Amplification Functions and response Spectra in Greece, *Journal of Earthquake Engineering*, 3, 237–270.

Lemoine, A., Bertil, D., Roullé, A., Briole, P., Foumelis, M., Raucoules, D. and de Michele, M., 2020. The volcano tectonic crisis of 2018 east of Mayotte, Comoros Islands. *Geophysical Journal International*, ggaa273, <https://doi.org/10.1093/gji/ggaa273>.

Liu, C., T. Lay, E. E. Brodsky, K. Dascher-Cousineau, and Xiong, X., 2019. Coseismic rupture process of the large 2019 Ridgecrest earthquakes from joint inversion of geodetic and seismological observations. *Geophysical Research Letters*, 46, 11820–11829.

- Marchetti, P.G., Rivolta, G., D'Elia, S., Farres, J., Mason, G. and Gobron, N., 2012. A Model for the Scientific Exploitation of Earth Observation Missions: The ESA Research and Service Support. *IEEE Geoscience and Remote Sensing*, 162, 10-18.
- Margaris, B. N., and Boore, D. M., 1998. Determination of  $\Delta\sigma$  and  $k_0$  from Response Spectra of Large Earthquakes in Greece. *Bulletin of the Seismological Society of America*, 88, 170–182.
- Motazedian, D., and Atkinson, G. M., 2005. Stochastic Finite-Fault Modeling Based on a Dynamic Corner Frequency. *Bulletin of the Seismological Society of America*, 95(3), 995-1010, doi:10.1785/0120030207.
- Novotny, O., Zahradnik, J., and Tselentis, G.-A., 2001. Northwestern Turkey Earthquakes and the Crustal Structure Inferred from Surface Waves Observed in Western Greece. *Bulletin of the Seismological Society of America*, 91, 875–879.
- Papadimitriou, E. E., 2002. Mode of strong earthquake occurrence in central Ionian Islands (Greece). Possible triggering due to Coulomb stress changes generated by the occurrence of previous strong shocks. *Seismological Society of America*, 92, 3293–3308.
- Papadimitriou, E.E., Karakostas, V.G., 2003. Episodic occurrence of strong ( $M_w \geq 6.2$ ) earthquakes in Thessalia area (central Greece). *Earth Planetary Science Letters*, 215, 395–409.
- Papadimitriou, E., Karakostas, V., Mesimeri, M., Chouliaras, G., Kourouklas, Ch., 2017. The  $M_w 6.7$  17 November 2015 Lefkada (Greece) earthquake: structural interpretation by means of aftershock analysis. *Pure Applied Geophysics*, 174, 3869–3888, DOI 10.1007/s00024-017-1601-3.
- Papanikolaou, I.D., Foumelis, M., Parcharidis, I., Lekkas, E.L. and Fountoulis, I.G., 2010. Deformation pattern of the 6 and 7 of April 2009,  $M_w=6.3$  and  $M_w=5.6$  earthquakes in L' Aquila (Central Italy) revealed by ground and space based observations. *Natural Hazards & Earth System Science*, 10, 73-87.
- Papazachos BC, Scordilis EM, Panagiotopoulos DG, Papazachos CB, Karakaisis GF (2004) Global relations between seismic fault parameters and moment magnitude of

earthquakes. *10<sup>th</sup> Congress Hellenic Geological Society*, Thessaloniki, Greece, 14–17 April 2004, 539–540.

Paradisopoulou, P. M., Papadimitriou, E. E., Karakostas, V. G., Taymaz, T., Kilas, A. and Yolsal, S., 2010. Seismic hazard evaluation in western Turkey as revealed by stress transfer and time-dependent probability calculations. *Pure Applied Geophysics*, 167, 1013–1048, doi:10.1007/s00024-010-0085-1.

Pavlidis, S., Chatzipetros, A., Sboras, S., Kremastas, E., Chatziioannou, A., 2021. The northern Thessaly strong earthquakes of March 3 and 4 and their neotectonic setting. <https://doi.org/10.5281/ZENODO.4618188>

Schaff, D. P. and Waldhauser, F., 2005. Waveform cross-correlation-based differential travel-time measurements at the northern California seismic network. *Bulletin of the Seismological Society of America*, 95, 2446–2461.

Schaff, D. P., Bokelmann, G. H. R., Ellsworth, W. L., Zankerka, E., Waldhauser, F. and Beroza, G., 2004. Optimizing correlation techniques for improved earthquake location. *Bulletin of the Seismological Society of America*, 95, 705–721.

Somerville, P., K. Irikura, S. Sawada, D. J. Wald, N. Abrahamson, Y. Iwasaki, T. Kagawa, N. Smith, and Kowada, A., 1999. Characterizing crustal earthquake slip models for the prediction of strong ground motion. *Seismological Research Letters*, 70, 59–80.

Stewart, J. P., Klimis, N., Savvaidis, A., Theodoulidis, N., Zargli, E., Athanasopoulos, G., Pelekis, P., Mylonakis, G., and Margaritis, B., 2014. Compilation of a Local VS Profile Database and Its Application for Inference of VS30 from Geologic- and Terrain-Based Proxies. *Bulletin of the Seismological Society of America*, 104(6), 2827–2841. <https://doi.org/10.1785/0120130331>

Takaku, J., Tadono, T., Tsutsui, K. and Ichikawa, M., 2018. Quality Improvements of ‘AW3D’ Global DSM Derived from ALOS PRISM, Proc. IGARSS2018, IEEE, Valencia, Spain, 1612–1615.

Tsodoulos, I., Chatzipetros, A., Koukouvelas, I., Caputo, R., Pavlidis, S., 2016a. Palaeoseismological investigation of the Gyroni Fault (Thessaly, Central Greece). *Bulletin of the Geological Society of Greece*, 50, 552–562.

- Tsodoulos, I., Stamoulis, K., Caputo, R., Koukouvelas, I., Chatzipetros, A., Pavlides, S., Gallousi, C., Papachristodoulou, C., Ioannides, K., 2016b. Middle–Late Holocene earthquake history of the Gyroni Fault, Central Greece: Insight from optically stimulated luminescence (OSL) dating and palaeoseismology. *Tectonophysics*, 687, <https://doi.org/10.1016/j.tecto.2016.08.015>
- Valkaniotis, S., Papathanassiou, G., Ganas, A., Kremastas, E., Caputo, R., 2021. Preliminary report of liquefaction phenomena triggered by the March 2021 earthquakes in Central Thessaly, Greece. <https://doi.org/10.5281/ZENODO.4608365>
- Wang, R., 1999. A simple orthonormalization method for stable and efficient computation of Green's functions. *Bulletin of the Seismological Society of America*, 89, 733–741.
- Wang, K., Dreger, D. S., Tinti, E., Bürgmann, R., and Taira, T., 2020. Rupture Process of the 2019 Ridgecrest, California  $M_w$ 6.4 Foreshock and  $M_w$ 7.1 Earthquake Constrained by Seismic and Geodetic Data. *Bulletin of the Seismological Society of America*, 110, 1603–1626, doi: 10.1785/0120200108.
- Wald, D. J. and Allen, T. I., 2007. Topographic slope as a proxy for seismic site conditions and amplification. *Bulletin of the Seismological Society of America*, 97(5), 1379–1395, doi: 10.1785/0120060267.
- Wald, D. J., Quitoriano, V., Heaton, T. H., and Kanamori, H., 1999. Relationships between Peak Ground Acceleration, Peak Ground Velocity, and Modified Mercalli Intensity in California. *Earthquake Spectra*, 15(3), 557–564, <https://doi.org/10.1193/1.1586058>.
- Waldhauser, F., and Ellsworth, W. L., 2000. A double–difference earthquake location algorithm: method and application to the northern Hayward fault, California. *Bulletin of the Seismological Society of America*, 90, 1353–1368.
- Wegmüller, U., Werner, C., Strozzi, T., Wiesmann, A., Frey, O., and Santoro, M., 2016. Sentinel-1 Support in the GAMMA Software. *Procedia Computer Science*, 100, 1305–1312.

Wells DL, Coppersmith KJ, 1994. New empirical relationships among magnitude, rupture length, rupture width, rupture area, and surface displacement. *Bulletin of the Seismological Society of America*, 84, 974–1002.

Wessel, P., Smith, W. H. F., Scharroo, R., Luis, J. F. and Wobbe, F., 2013. Generic Mapping Tools: improved version released. *EOS Trans AGU* 94, 409-410.